FIRST PRINCIPLE INVESTIGATION OF Cs*X*Br$_3$ (*X*=Si, Ge) FOR SOLAR CELLS APPLICATIONS

JUMA KENNEDY WANYAMA

A Thesis Submitted to the Institute of Postgraduate Studies of Kabarak University in Partial Fulfillment of the Requirements for the Award of Master of Science in Physics Degree

KABARAK UNIVERSITY

NOVEMBER, 2025

DECLARATION

1. I do by declare that:

   i. This thesis is my work and to the best of my knowledge, it has not been presented for the award of a degree in any university or college.

   ii. That the work has not in-cooperated material from other works or a paraphrase of such material without due and appropriate acknowledgment

   iii. That the work has been subjected to processes of anti-plagiarism and has met Kabarak University 15% similarity index threshold

2. I do understand that issues of academic integrity are paramount and therefore I may be suspended or expelled from the University or my degree may be recalled for academic dishonesty or any other related academic malpractices.

Signed:________________________________ Date:______________________

Juma Kennedy Wanyama

GMP/M/0050/01/21

RECOMMENDATION

To the Postgraduate Studies Institute:

This thesis, entitled "**First Principle investigations of $CsXBr_3$ (X=Si, Ge) for Solar Cells Applications, "**written by **Juma Kennedy Wanyama ,** is presented to the Institute of Postgraduate Studies of Kabarak University. We have reviewed the thesis and recommend that it be accepted in partial fulfillment of the requirements for the award of the degree of Master of Science in Physics.

Signed:________________________________ Date:______________________

Dr. Phillip Otieno Nyawere

Department of Physical Sciences and Biological Sciences

Kabarak University

Signed:________________________________ Date:______________________

Dr. Elicah Wabululu

Department of Physical Sciences and Biological Sciences

Kabarak University

COPYRIGHT

ACKNOWLEDGMENT

This study could not have been completed without the valuable contributions of all those who sacrificed their time to offer assistance to me. First, I am grateful to my supervisors, Dr. Phillip Otieno Nyawere and Dr. Elcah Wabululu, for their scientific expertise, criticisms, guidance, and friendly assistance during my master's programme. Their suggestions were very pertinent at various stages of the research and the writing of the thesis.

I thank the Center for High-Performance Computing (CHPC) in Cape Town, South Africa, for providing a High-Performance Computing facility that was used for all the calculations in this thesis. Also, my appreciation goes to the Materials Science and Solar Energy Network for Eastern and Southern Africa (MSSESA) and Kabarak University for providing me with the platform to present my work, as well as networking with other researchers and workshops organized to give a wider understanding of DFT and the quantum ESPRESSO software, which greatly helped me in my research.

Finally, I acknowledge my wife, Delly, and my children, Warren, Scott, and Dency: It is their prayers, patience, and support that enabled the success of this work.

Any shortcoming therein is my responsibility.

DEDICATION

This study is dedicated to my parents for modeling me within a context of total want and for training me to be a character of total resilience.

ABSTRACT

Lead has been at the core of many recent studies on solar cells because it has unique properties that enhance light absorption and charge transport. Most of these studies are not practically employed due to the toxicity and instability of lead. This study focused on finding an alternative to lead that maintains or exceeds its performance in solar cells. The development of environmentally friendly, stable, and efficient perovskite materials for future solar cell applications has long-term practical significance and can eventually be commercialized. The current reported efficiency in $\mathrm{MAPbBr_3}$ is of the order of 22%, and this research aims to explore whether this efficiency could be improved beyond having lead in the crystal. It is for this reason that density functional theory, using the GGA-PBE and HSE06 correlation functionals, was employed on CsXBr3 (X=Si, Ge) to understand their optoelectronic properties and to calculate their efficiency as potential solar cell materials. The trends in electronic band structure in the cubic phase of $\mathrm{Cs}X\mathrm{Br}_3$ all-inorganic perovskites for X= Cs, Ge were determined. The absorption spectrum was calculated using a simplified mathematical function that approximated the real spectrum. Here, the absorption spectra of CsXBr3 (X = Si, Ge) perovskites were calculated at the quantum-mechanical level of accuracy using the DFT method. This realistic absorption spectrum was employed in Quantum Espresso and Siesta, with post-processing using the Yambo package. The materials exhibited optical absorption of over 10^5 cm in the ultraviolet spectrum. Determination of elastic, electronic, structural, and optical properties in the cubic stable phase of $\mathrm{Cs}X\mathrm{Br}_3$ (X=Si, Ge) was done, and the solar conversion efficiency of $\mathrm{Cs}X\mathrm{Br}_3$ (X=Si, Ge) were 11.02 % and 11.65 % respectively, under standard solar illumination conditions. The band gap of 0.7eV and the Poisson's ratio (ν) of 0.36 for $\mathrm{CsGeBr_3}$ were obtained. While for $\mathrm{CsSiBr}_{3,\ \mathrm{the}}$ band gap of 0.29 eV and Poisson's ratio (ν) of 0.255 were obtained. Dielectric constants, which include the real (ε_1) and imaginary part (ε_2) of $\mathrm{CsGeBr_3}$ and $\mathrm{CsSiBr}_{3,}$ were 2.0 eV and 2.7 eV, and the absorption begun from 2.5eV to match the band gap. The results obtained can be used in experimental research to develop CsGeBr3 and CsSiBr3 materials as potential high-performance solar cells with higher efficiencies and good performance, and to verify experimentally the use of $\mathrm{CsGeBr_3}$ and $\mathrm{CsSiBr_3}$ perovskites in solar cells. The results are significant in determining a suitable solar cell material for industrial applications. The study dealt only with theoretical findings on the structural, electronic, dielectric, and elastic properties of CsGeBr3 and CsSiBr3 at ground-state conditions. The structures were optimized using the Murnaghan equation of state in LUNA Quantum Espresso. It was concluded that the cubic phase of $\mathrm{CsGeBr_3}$ and $\mathrm{CsSiBr_3}$ are suitable materials for solar cell materials because of their suitable band gap. An extension of this work could be to use other exchange-correlation functionals.

Keywords: *Solar Cell, First Principle, Density Functional Theory, Perovskites, Quantum Espresso, Siesta.*

TABLE OF CONTENTS

LIST OF TABLES

LIST OF FIGURES

LIST OF ABBREVIATIONS AND ACRONYMS

CASTEP	Cambridge Sequential Total Package
DFT	Density Functional Theory
DOS	Density of State
EoS	Equation of State
E	Electronic Charge
E_g	Band Gap
ESPRESSO	Open Source Package in Electronics
GGA	Generalized Gradient Approximation
H	Total Hamiltonian
KS	Kohn-Sham
PAW	Projected Augmented Wave
PAW	Perdew-Burke-Ernserhof
Pb	Lead
PL	Photoluminescence
PCE	Power Conversion Efficiency
SIC	Self-Interaction Correlation
SIESTA	Spanish Initiative for Electronic Simulation with Thousands of Atoms

OPERATIONAL DEFINITION OF TERMS

Band Gap: This is the energy between the valence band maximum of electrons and the conduction band minimum of a solid material for an insulator or a semiconductor, and consists of the range of energy values that are forbidden to electrons in the material.

Electronic Properties: These are parameters and representations that show how electrons behave within a substance.

Optical Properties: The material's response to incident radiation is characterized by reflectance, refraction, transmittance, and absorption.

Mechanical Properties: These are the physical properties exhibited by a material upon application of forces. These properties include the tensile strength, modulus of elasticity, and elongation.

Photoelectric Effect: This is a phenomenon in which electrically charged particles are released from or within the material when light falls on it.

Photoelectron: This is an electron emitted from an atom by an interaction with a photon, especially by the action of light.

Photoluminescence: This is the process by which photons or light energy stimulate a photon’s emission. A photon may also be emitted by fluorescence, which elevates a particle to an excited electronic state.

Solar Cell: This is an electrical device that converts light energy directly into electricity through the photovoltaic effect.

Young’s Modulus: This characteristic, which is defined as the ratio of malleable pressure measure of power applied per unit area) to tensile strain (the material's ability to stretch and twist effectively).

Bulk Modulus: This is the total change in a body's volume caused by a constant, unit compressive force operating across the surface, or an elastic pressure.

Shear Modulus (G): It is defined as the ratio of shear pressure to shear strain and represents the fraction of a material's versatile shear firmness.

Anisotropy Factor (E): This has a probability thickness and a single dissipating course acting as a boundary. It is the normal of the cosine of the dissipating point.

CHAPTER ONE

INTRODUCTION

1.1 Introduction

This section discusses the background of the concepts of solar cells and the problems to be addressed for the application of $CsSiBr_3$ and $CsGeBr_3$ in solar cells. It then proceeds to state the research problem, outline the objectives and research questions to be addressed, and define the study's significance, scope, and assumptions.

1.2 Background to the Study

Perovskite is a term given to all compounds that have the general chemical formula ABX_3 and the crystal structure of calcium titanate, $CaTiO_3$. They are Organic-inorganic metal halide perovskites, where A is an organic cation, B is a divalent metal ion, and X is a halide such as $CH_3NH_3Pb_3$ (Methylammonium lead halide). Organic-inorganic hybrid perovskite (OIHP) has an ABX3 Structure, where A is methylammonium (MA), cesium (Cs), or formamidinium (FA); B is Pb or Sn; and X is I, Cl, or Br (Yu-Ling Sun et al., 2017). High optical absorption coefficient, high carrier mobility, and long carrier diffusion length are significant factors that support OIHP's high efficiency. Currently, the efficiency of perovskite solar cells exceeds that of well-established technologies such as copper-indium-gallium-selenide (CIGS) and cadmium-telluride (CdTe) due to a multilayer coating (Yang, 2016).

However, the high cost of fabricating single-crystalline silicon (sc-Si) has accelerated recent research on next-generation thin-film solar cells to find a solar cell material that is cheaper and less toxic than silicon. Electronic and optical properties of perovskites have been broadly explored by first-principles calculations based on density functional theory (Wang, 2014). Optical activity in a crystal plays a fundamental role in electronic structure theory and is highly dependent on the electronic band gap (Ling, 2017). Due to the self-interaction error, most electronic structure methods underestimate the electronic band gap and thus poorly define the optical activity in a crystal (Zekry, 2019). As an option to avoid self-interaction errors in DFT, Zhu and co-workers (2014) applied quasi-particle corrections via the GW approach to achieve a realistic DFT description of the orthorhombic and tetragonal $MAPbI_3$ band gaps.

Solar cells based on hybrid organic-inorganic lead-halide perovskites have significantly increased in efficiency in recent years. Lead is toxic, so the primary challenge with this material is to replace lead in the perovskite crystal with a less toxic, more efficient metal. This has led to the search for related compounds that may replicate the properties of hybrid lead-halide perovskites, which are less toxic and more efficient (Noel *et al.,* 2014), hence the need for this study.

First-principles computation is a quantum-mechanical method that aims to solve the electronic Schrödinger equation using the positions of the nuclei and the number of electrons in the system. This numerical simulation is essential in exploring structural, electronic, elastic, and optical properties. The studies by Babkin *et al.* (2011) point out that band-structure calculation is an effective theoretical tool for predicting such properties. This study endeavors to employ first-principles calculations on the elastic, electronic, and optical properties of CsGeBr3 and CsSiBr3 to assess their suitability for solar cell applications.

1.3 Statement of the Problem

The problem in this work is two-fold: (i) Lead has been at the core of many studies on solar cells in the recent past. It has portrayed excellent performance theoretically. Most of these studies are not practically employed due to the toxicity and instability of lead (Madeeha, 2020). This study focused on finding an alternative to lead that maintains or exceeds its performance. The development of environmentally friendly, stable, and efficient perovskite materials for future photovoltaic applications has long-term practical significance and can eventually be commercialized, hence the need for this study. (ii) The current reported efficiency in $MAPbBr_3$ is of the order of 22%, which this work explored whether this efficiency could be improved, but beyond having lead in the equation. It is for this reason that first-principles calculations were employed on CsXBr3 (X=Si, Ge) to elucidate their stability, elastic and optical properties, and to assess their efficiency as potential solar cell materials.

1.4 Objectives

The main objective of this study was to determine the structural, elastic, electronic, and optical properties of CsXBr3 (X = Si, Ge) for solar cell applications using Density Functional Theory.

1.4.1 Specific Objectives

The specific objectives of this study were to;

i. Determine the stable phase of CsXBr3 (X = Si, Ge) using density functional theory, with practical applications as solar cell materials.

ii. Compute the elastic constants of the cubic phase of $CsXBr_3$ (X=Si, Ge) and their application to solar cells using density functional theory.

iii. Determine the electronic structure of the cubic phase of $CsXBr_3$ (X=Si, Ge) and their application to solar cells using density functional theory.

iv. Study the optical properties of the cubic phase of $CsXBr_3$ (X=Si, Ge) using density functional theory and its application to solar cells.

1.5 Research Questions

In order to guide this study, the following research questions were used:

i. Which is the stable phase of $CsXBr_3$ (X=Si, Ge) that will have practical applications as solar cell materials?

ii. What are the values of the elastic properties of the cubic phase of $CsXBr_3$ (X=Si, Ge) that will render these materials suitable for solar cells?

iii. What are the electronic structure properties of the cubic phase of $CsXBr_3$ (X=Si, Ge) that make these materials suitable for solar cells?

iv. What are the optical properties of the cubic phase of $CsXBr_3$ (X=Si, Ge) in comparison to other studies that will render them suitable for solar cells?

1.6 Significance of the Study

The properties under study were elastic, optical, and electronic, which are used in solar cell devices according to Burgelman et al. (2004). The study will provide significant information for the design of less toxic, more efficient solar cell devices. It will also provide vital information to experimentalists and fabricators of solar cells on the elements to be employed to achieve a stable solar cell, as compared to lead-based cells, which are unstable and toxic, and whether this type of perovskite will exhibit a longer lifespan and higher current density.

1.7 Justification of the Study

While there is much published work on perovskites related to inorganic-organic compounds, there is insufficient literature on all inorganic perovskites with lead as an element in the equation. The toxicity of lead, along with its low efficiency below 22%, has intensified research aimed at developing environmentally friendly solar cell materials with efficiency above 22%. This will have applications in electronics, solar technology, and optoelectronics. Therefore, by conducting this study on the performance of CsXBr$_3$ (X=Si, Ge) for solar cell applications to replace lead in the equation, it is expected that the results will serve as an essential consideration for experimentalists and solar cell manufacturing companies when designing solar cell materials. The study shows that the cubic phase of Ge and Si halide perovskite can be used in solar cell fabrication. The results of this study should therefore serve as an alternative to the experimental fabrication of Ge- and Si-based halide perovskites for solar cells. It is further expected that the study's results will contribute to the body of knowledge regarding $CsGeBr_3$ and $CsSiBr_3$ halide perovskites.

1.8 Scope of the Study

This study focused on the elastic, optical, electronic, and dielectric properties of CsSiBr3 and CsGeBr3.The findings are crucial for determining the solar-cell applications of all-inorganic halide perovskites. Computational modeling methods based on Density Functional Theory (DFT) were used and limited to the cubic phase of these perovskites. Quantum ESPRESSO was used to study electronic properties; the Siesta code was used to study Optical and mechanical properties, and Thermo_pw was used to study elastic properties.

All the calculations were done at 0K and 0Gpa. The Plane Waves, as implemented in the Quantum ESPRESSO code, were used as the basis sets. The study focused only on the cubic phase of these structures after ascertaining its stability. The distortions were mild to remain within the structure.

1.9 Assumptions

The following presumptions were made:

i. Analysis was performed using the plane wave formalism in DFT calculations in the Quantum ESPRESSO code, which was utilized in obtaining the desired material properties.

ii. Data and information on the properties of $CsGeBr_3$ and $CsSiBr_3$ and other similar works would be available for comparison.

iii. The time for the research would be sufficient to give answers to the stated objectives.

CHAPTER TWO

LITERATURE REVIEW

2.1 Introduction

This chapter discusses the properties of inorganic-inorganic perovskites that are relevant to their applications in solar cells. Literature on elastic, structural, electronic, optical, and the insight of power conversion efficiency will be discussed. The Conceptual framework will also be presented and discussed.

2.2 Perovskites for Solar Cells

Perovskites are a group of crystals that exhibit characteristics for applications in nanotechnology, especially nanostructured solar cells (Logothetidis, 2012). They are found as oxides and non-oxides, with silicates being the most common, but they also occur as fluorides, arsenides, and intermetallic compounds. While natural perovskite minerals are few, synthetic perovskites cut across the periodic table in terms of composition of elements, and they can exist in complex formulas such as metallic perovskites, hybrid organic–inorganic perovskites, metal-free perovskites, and even inert gas-based perovskites. These materials are usually inexpensive to produce and easy to manufacture. They have a broad absorption spectrum, fast, long-range electron and hole transport, and long carrier separation lifetimes as their intrinsic properties, making them suitable materials for solar cells (Logothetidis, 2012).

Perovskites exhibit an atomic arrangement in a 3-dimensional array of corner-sharing octahedra. Conversely, layered perovskites consist of 2-dimensional layers of corner-sharing octahedra separated by cation layers. Hence, the electronic energy bands of perovskites and layered perovskites are unusual, and their structure is unique (Atta *et al*, 2016) as in figure 1 below;

Figure 1

Octahedral Structure of Perovskites

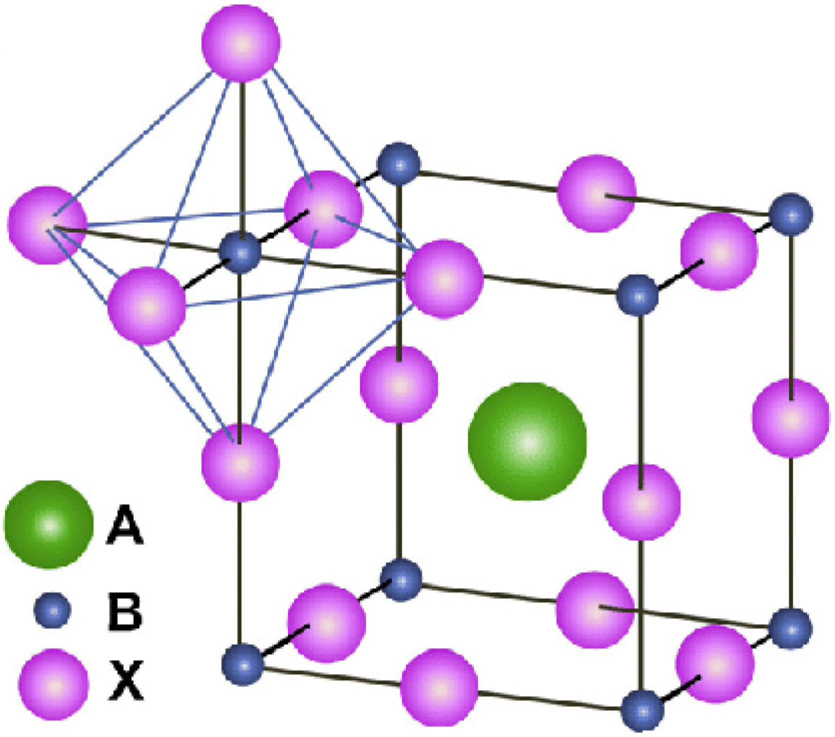

Inorganic-organic $CH_3NH_3PbI_3$-based perovskite solar cells have been widely studied because, after conversion efficiency reached 15% in 2013, higher efficiencies have been achieved across various processes and device structures, with conversion efficiency exceeding 20% (Gao *et al*., 2023).

With rapid progress in power conversion efficiency (PCE) to reach 25%, metal halide perovskite-based solar cells became a game-changer in the photovoltaic performance race. The characteristic features of perovskite materials may enable further advancement of PCE beyond that afforded by silicon solar cells toward the Shockley–Queisser limit (Young *et al*., 2011).

Lead-based perovskite material toxicity, device hysteresis, and perovskite material stability are major challenges that need to be overcome for it to be practically applied in real life. Challenges posed by environmental factors such as moisture, oxygen, temperature, and light remain unanswered. The lead toxicity of PSCs demands a lead substitute with no compromise in their efficiency.

2.3 Solar Cell Structure and Mechanism

A solar cell is an electronic device that directly converts sunlight into electricity. Light shining on the solar cell produces both a current and a voltage, generating electric power. This process requires, first, a material in which light absorption raises an electron to a higher energy state, and second, the movement of this higher-energy electron from the solar cell into an external circuit. The electron then dissipates its energy in the external circuit and returns to the solar cell. A variety of materials and processes can potentially satisfy the requirements for photovoltaic energy conversion. However, in practice, nearly all photovoltaic energy conversion uses semiconductor materials in the form of a *p-n* junction.

Figure 2

Solar Cell Structure

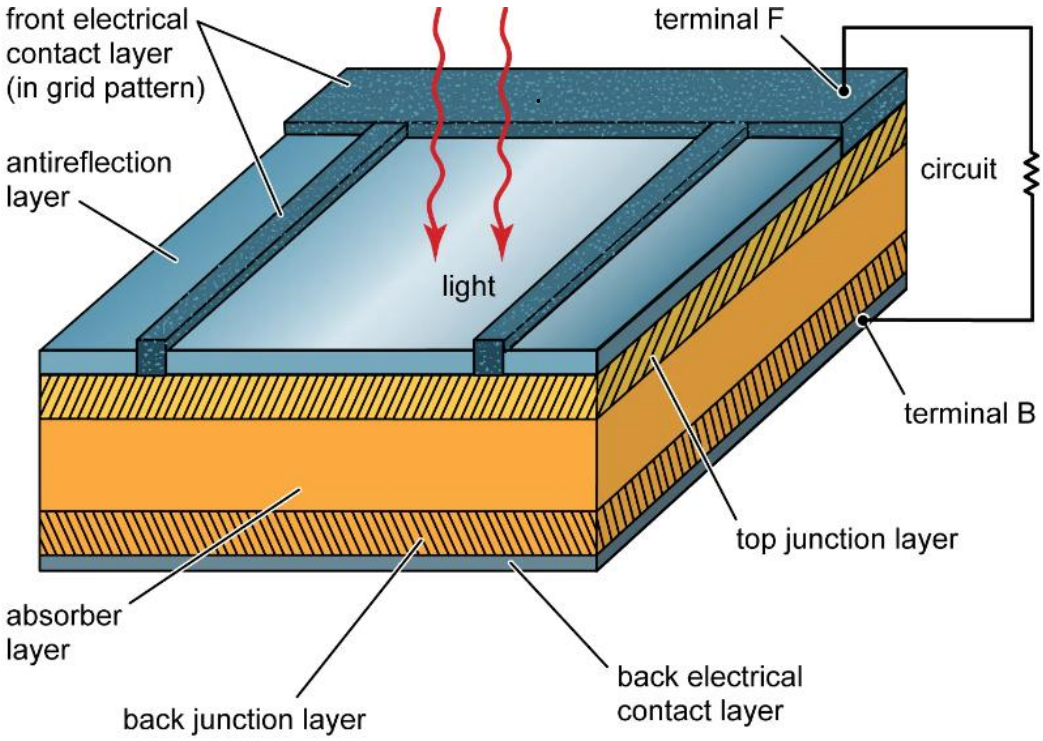

Figure 2 above depicts a commonly used solar cell structure. The absorber layer and the back junction layer are both made from the same material. Light enters the device through an optical coating, or antireflection layer, which minimizes reflection losses and effectively traps light incident on the solar cell by promoting its transmission to the energy-conversion layers.

2.4 Solar Materials Beyond Lead

The toxicity of lead-based halide perovskites hinders their large-scale commercial use in solar cells. Perovskite solar cells (PSCs), as a promising category of solar cells, have attracted attention in the past due to their high absorption coefficient, bipolar charge mobility, long carrier diffusion length, low exciton binding energy, low trap-state density, and tunable band gap (Xing *et al*. 2013).

Filip *et al*. (2014) considered stability and the desired band gap as two factors for suitable lead-free perovskite materials. They used random structures (atom positions and lattice parameters) to investigate the stability of possible lead-free perovskites. Considering stability and the band gap as significant factors, the crystal structure retains the perovskite geometry after relaxation, and the relativistic band gap is less than 2.0eV. In subsequent research, it was shown that Cu, Ag, Bi, and Sb can also replace Pb to form perovskites. This study replaced Pb with Si and Ge. To maintain charge neutrality, the heterovalent replacement can be divided into three subcategories: cation splitting, mixed-valence anion, and ordered vacancy. Cation splitting is used to form a double perovskite structure. The perovskite can maintain electrical neutrality by forming ordered vacancies.

Many theoretical studies have been conducted on Pb replacement with various elements, e.g., Sn and Bi. These studies reveal the merits and demerits of different lead-free perovskite materials. In the process of studying the optoelectronic properties of $MASnI_3$ using the GW + SOC method, the researchers found that compared with $MAPbI_3$, $MASnI_3$ showed a stronger s-p antibond coupling near the maximum value of the valence band (Varmo P.C.,2018). This occurrence was because the Sn 5s lone pair is shallower and more active than the Pb 6s lone pair. As a result, the band gap of MASnI3 is lower than that of MAPbI3.

2.5 Ge-Based Perovskite Materials

Ge could be a suitable substitute for Pb as a new type of lead-free perovskite material. Band gaps of the Ge-based perovskites can be tuned to values close to those of conventional lead halide photocells (1.5 eV) by altering A-site cations (Bitnar, 2014).

Kanatzidis *et al*. (2015) examined a series of AGeI3 perovskite compounds and characterized their structural, electronic, and optical properties. The band gaps of the Ge-based perovskites increase with the increased radius of the A-cation. For instance, $CsGeI_3$ has an optical band gap of 1.63 eV, whereas other $AGeI_3$ perovskites universally exhibit wide band gaps of ≥2.0 eV (Khan et al., 2013). This study endeavors to ascertain whether CsGeBr3 and CsSiBr3 have a band gap wider than this and to determine their suitability for the absorption of ultraviolet radiation.

Kanatzidis *et al.* (2015) used the pyramidal [GeI3] building block to synthesize a series of Ge-based perovskites and to replace their A-site cations. The experimental data showed that $CsGeI_3$, $MAGeI_3$, $FAGeI_3$, and CH3C(NH2)2GeI3 were 3D perovskite structures with direct band gaps of 1.6, 1.9, 2.2, and 2.5 eV, respectively. At the same time, $C(NH_2)_3GeI_3$, $(CH_3)_2C(H)NH_3GeI_3$, and $(CH_3)_3NHGeI_3$ were 1D infinite chain structures separately with indirect band gaps of 2.7, 2.5, and 2.8 eV. $CsGeI_3$ exhibited the highest optical absorption coefficient and demonstrated greater application potential in the photovoltaic field.

Ran *et al.* (2009) reported a uniform, pinhole-free (CH3NH3)3Bi2I9 thin film via a two-step evaporation spin. They optimized film-forming conditions by comparing the integrated current from IPCE measurements and formed packed $(CH_3NH_3)_3Bi_2I_9$ thin films. Using this strength, they manufactured an inverted planar heterojunction photovoltaic device with a PCE of 0.39% and a high V_{oc} of 0.83 V, which gave the lowest loss-in-potential to date in $(CH_3NH_3)_3Bi_2I_9$-based solar cells. Park *et al.* (2015) developed more efficient solar cells using MA cations in Bi-based perovskite in place of Cs cations. Based on that research, Johansson *et al.* used Cs3Bi2I9, a bismuth halide, as the light absorber in their solar cells.

Although researchers have achieved positive results with Bi-based perovskites, the performance of their perovskite solar cells remains low due to their large band gaps, large carrier effective masses, high exciton binding energies, increased internal defects, and defect intolerance. This current study focuses on finding an alternative to lead that maintains or surpasses its performance. The current reported efficiency in $MAPbBr_3$ is of the order of 22%, and this research aims to explore whether this efficiency can be improved. It is for this reason that this study employed first-principles calculations on CsXBr3 (X = Si, Ge) to understand their optoelectronic properties and to assess their performance as potential solar materials.

2.6 Si-Based Perovskite Materials

A silicon-based perovskite was investigated within the framework of density functional theory (DFT) for application in solar energy harvesting technology. The DFT calculations were carried out at the GGA-PBEsol and GGA-HTCH/407 levels of theory to explore the structural, electronic, and optical properties of the silicon hybrid organic-inorganic perovskite, CH3NH3SiI3 (MASiI3), and the results were compared with those of the popular Pb-containing perovskite, $CH_3NH_3PbI_3$ ($MAPbI_3$). The structure of

$MASiI_3$ is reported as cubic based on a Goldschmidt tolerance factor of 0.93, which falls within the range for the formation of stable cubic perovskites. It is found that $MASiI_3$ is a direct-band-gap semiconductor exhibiting n-type extrinsic behavior. The optical activities indicate intense absorptions in the ultraviolet and visible regions, which are needed for high photovoltaic activity.

The high absorption coefficient of $MASiI_3$ in the 105 region is comparable to that of MAPbI3, indicating that the active absorber layer can be structured into a thin film for high-power-efficiency conversion. The results of this study imply that perovskite absorbers can incorporate silicon (Si) instead of lead (Pb) to eliminate Pb toxicity, which raises environmental concerns in hybrid organic-inorganic perovskites (HOIPs).

Many modifications were explored to promote the development of Si-based solar cells in In order to attain lower fabrication costs. These include structures with micro-gratings which have vertical sidewall emitter contacts (Yang, 2012), micro-pillars with Cu nanoparticles (Zhang, 2018), nanorods with a high-doped pn-junction in the radial path (Garnett, 2008), and npn microstructure based on high-doped wafers (Salem *et al,*2008), among other structures. However, other counterparts are being investigated to achieve an optimum efficiency-to-cost ratio. In this regard, many promising materials have been recognized for potential use in thin-film solar cells (TFSCs). These materials reveal high PCEs, for example, over 25% for perovskite, 21% for CdTe, 23% for copper indium gallium selenide (CIGS), and 19% for organic TFSCs (UNIST, 2021). Among these materials suitable for TFSCs, perovskite and organic materials have attracted many researchers owing to their common advantages, including low cost, low-temperature solution processing, and simple fabrication steps (Chen et al., 2021).

2.7 Structural and Electronic Properties of Perovskite Materials

The perovskite solar cell first reported a PCE of 2.2% (Miyasaka *et al.*, 2006), which reached 3.8% in 2009. In 2018, a research report on a PCE of 27.6% was published, stating that a PCE of 30% or more was possible by the end of 2020, but in 2020, the US National Renewable Energy Laboratory certified a perovskite solar cell with a max. PCE of 25.5%. Researchers found hope for mixed halide perovskites from a comparative study of different structures. Thus, organic-inorganic lead halide perovskite solar cells have drawn incredible attention in the scientific community as alternative competitors to some inorganic photovoltaic materials, such as copper-indium-gallium-sulfide-selenide (CIGS), cadmium telluride (CdTe), amorphous or single-crystal silicon (a-Si or c-Si), iron disulfide (FeS_2), and gallium arsenide (GaAs). Though multi-junction AlGaInP, AlGaAs, GaAs, and GaInAs cells are certified as 47.1% efficient in the present research (Geisz et al., 2020), all of these compounds are expensive due to the presence of scarce elements, In and Ga, and they are also toxic as they contain As and Pb. Hence, metal halide perovskite solar cells have a great potential to replace the dominant Si-based solar cells by proper selection of atoms in the right place (Zhang, 2016).

The three phases (cubic, tetragonal, and monoclinic) of CsGeBr3 were primarily chosen as the highest-temperature phases of the cubic structure to perform numerical operations for high-temperature device applications. The optimized-cell structure of $CsGeBr_3$ was determined, and then the Br atom was replaced by C1 and 1 atoms, which were then optimized for $CsGeBr_3$ and $CsSiBr_3$ perovskite structures, as shown in Figure 3 below.

Figure 3

The Cubic Phase of $CsGeBr_3$ and $CsSiBr_3$ represented as balls and sticks.

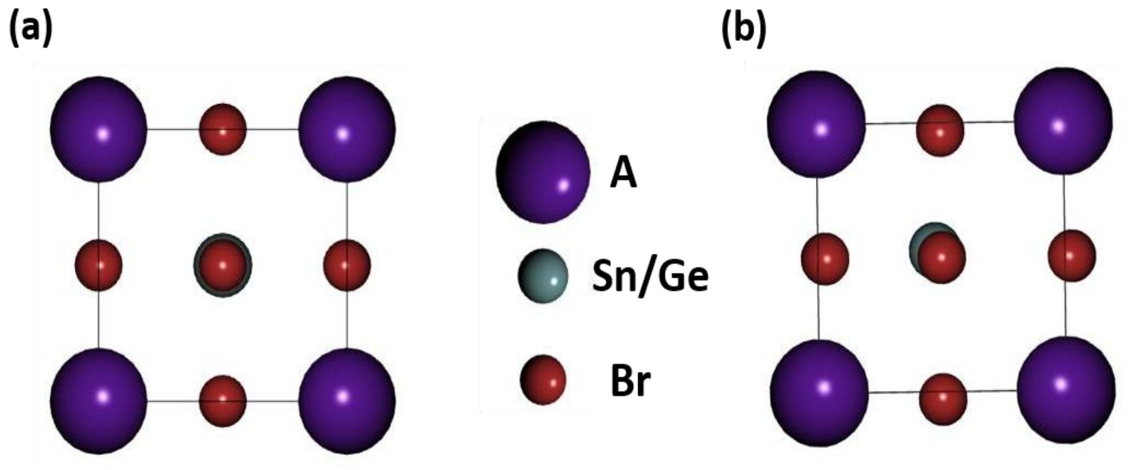

Nonetheless, the present investigation guarantees that multi-junction AlGaInP, AlGaAs, GaAs, and GaInAs cells are 47.1% effective (Geisz J.F *et al.*, 2020). Due to the lack of components, In and Ga, all of these compounds are expensive and toxic. Additionally, because they contain As and Pb, which are toxic. As a result, by properly placing atoms in the right positions in the structure, metal halide perovskite solar cells have a good opportunity to replace the dominant Si-based solar cells (Zhang, 2016).

2.8 Elastic Properties of All Inorganic Perovskites for Solar Cell Application

The crystallinity and stress state of the perovskite layer can strongly affect the absorption performance of the perovskite solar cell, and the elastic properties of the perovskite layer material can reveal its strain, stress, fracture mechanics, and deformation. So, it is necessary to analyze the elastic properties of perovskite in the system for practical applications (Krishnamoorthy, 2015). Elastic properties describe the mechanical behavior of materials under strain. The elastic constants C_{ij} are obtained by calculating the total energy as a function of volume-conserving strains using the Mehl method (Rai, 2017). According to the obtained elastic constants, the other interesting elastic properties for applications such as elastic anisotropic factor (A), bulk modulus (B), shear modulus

(G), Young’s modulus (E), and Poisson’s ratio (ν) can be obtained.

2.9 Optical Properties of Perovskite and Applications in Solar Cells

Many application fields, such as absorbers, reflectors, optical coatings, and various optoelectronic devices, are examined based on their optical responses. In the presence of an external electromagnetic wave, the photonic interactions of the material can provide information on the properties and application predictions as a function of energy. These properties are analyzed for electronic transitions between occupied and empty states, band structures, bond types, and the internal structures of the materials based on their optical spectra. The Kramers follows the frequency-dependent complex dielectric function–Kronig transformation as $\varepsilon(\omega) = \varepsilon_1(\omega) + i\varepsilon_2(\omega)$, which is also related to the representation of relative permittivity. The imaginary part of this complex function is,

$$\varepsilon_{2.}(\omega) = \frac{2e^2\pi}{\Omega\varepsilon_0} \sum_{k,v,\lambda} k\psi_k^c \left|\psi_k^c\right|^2 \delta(E_k^c) - E_k^c - (E) \qquad \text{... (1)}$$

where $\omega = 2\pi v$ is the frequency of the incident photon and e is the electronic charge. Whereas, Ψ_k^c and Ψ_k^v are the wave functions of the conduction and valence bands at K, respectively. Using ε_1 and ε_2, other optical properties such as absorption coefficient $\alpha(\omega)$, optical conductivity $\sigma(\omega)$, loss function $L(\omega)$, reflectivity $R(\omega)$, and refractive index $n(\omega)$ can be calculated.

2.10 Photovoltaic Application of Perovskite

In establishing the photovoltaic applicability of perovskite solar cells, Granas et al. (2016) investigated the impact of the perovskite structure on photovoltaic performance in the presence of different ions at the A, B, and X sites, using electronic structure calculations. Their results showed that the level of alignment between the electron- and hole-transporting media is key to achieving maximum efficiency in heterogeneous positive-intrinsic-negative (PIN) junctions. Low-dimensional perovskite formed by replacing small hydrophilic cations with much bulkier organic ones can improve the stability of Hybrid Perovskite Solar Cells (HPSCs) upon exposure to moisture. The preferential crystal orientation and high degree of crystallinity are fundamental to improving solar cell performance. The 2D/3D-based Hybrid Perovskite Solar Cells are highly stable upon exposure to light or ambient conditions, due to the enhanced robustness of the perovskite film.

The power conversion efficiency of perovskite solar cells is high, depending on the chemical composition of the perovskite layer and the electronic structure properties of the electron- and hole-transporting media, as predicted by the Shockley-Queisser triangle (Muhammad et al., 2019). Other approaches will result in lower power conversion efficiency.

2.11 Properties, Advantages, and Challenges of Perovskite Solar Cells

Some of the properties of organic-inorganic hybrid perovskite materials that make them potentially applicable to solar cell devices include: first, their light-harvesting characteristics and good hole-transporting properties (Liu *et al*., 2013). Secondly, the printing techniques that use low-temperature solar cell processing enable deposition on a flexible substrate (Fan *et al*., 2014). Thirdly, low energy loss due to increased light absorption, thereby increasing photo-generated free charge carrier generation. This enables charges to be generated, thereby increasing charge collection at the electrodes (Stranks *et al*., 2013). Lastly, low processing cost and high efficiency, which means a low energy payback time.

Despite the aforementioned advantages of organic-inorganic hybrid perovskites, perovskite solar cells still face several challenges that hinder their large-scale commercial use. These challenges include, but are not limited to: First, lead, one of the most widely used elements in perovskite solar cells, is toxic and unstable. Hence, environmentally friendly materials such as silicon and germanium have recently been proposed as alternatives to lead perovskites for solar cell applications. Secondly, perovskite materials are crystalline, thus extremely sensitive to humidity and dissolve easily. However, it has been addressed by preparing them under an inert atmosphere, as described by Mitzi et al. (1995). It is then followed by encapsulating the whole device within the air-tight sealant in the same inert condition. This is not cost-effective for large-scale production; however, it has been used to reduce the degradation and oxidation of Sn 2+ to Sn 4+, thereby increasing the lifetime of tin perovskite solar cells for up to 4 months (Noel *et al.*, 2014). Lastly, sequential deposition of the constituent perovskite materials has been used to obtain a continuous film over a larger area without degradation of cell efficiency (Burschka *et al.*, 2013).

2.12 Research Gaps

Lead has been at the center of most solar cell devices because of its lower soldering temperatures, superior photovoltaic properties, and high optical absorption coefficient. However, its toxicity and its presence in isotopes have limited its use on a large scale. Also, the reported efficiency is of the order 25.5% which this study explored, showing that higher efficiency can be obtained by substituting lead with germanium or silicon in the equation. The optimum bandgap energy Eg for a single-junction solar cell is 1.34 eV under AM 1.5G solar illumination, with a PL quantum efficiency of 100%, as derived from detailed balance theory.

2.13 Conceptual Framework

Figure 4

Conceptual Framework

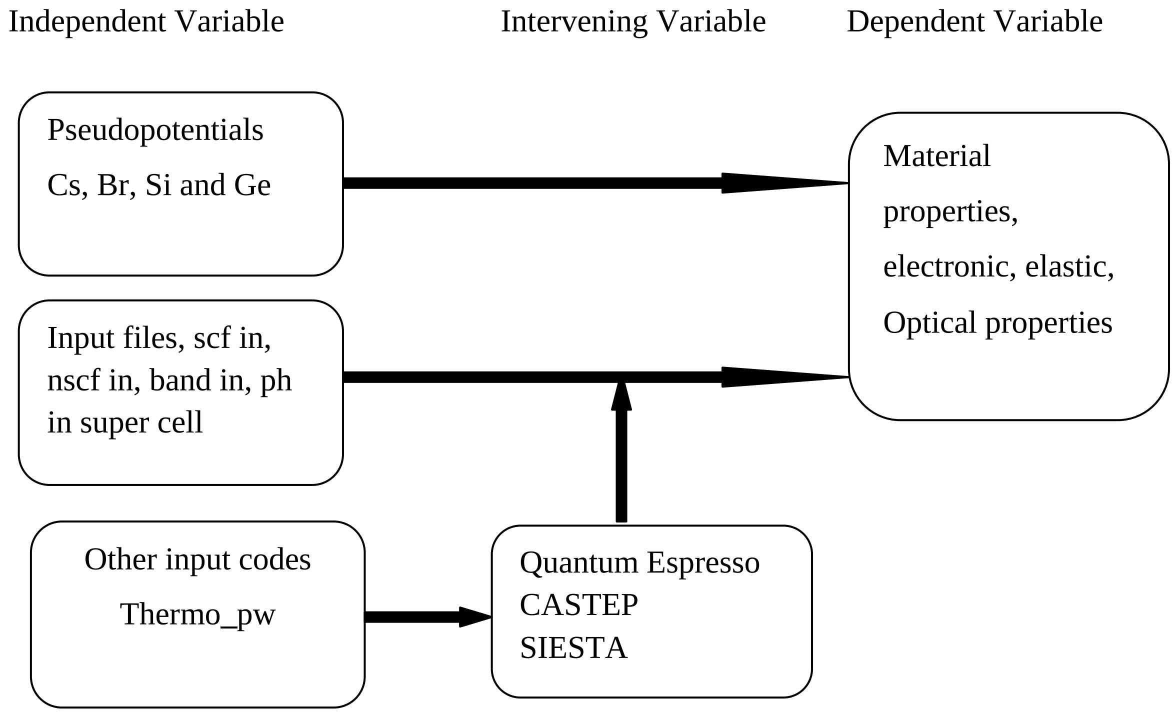

Source: Researchers own conceptualization

Figure 4 above illustrates the conceptual framework. It has three sets of variables: the dependent, independent, and intervening variables. The independent variables are the material properties obtained from the input files, the pseudopotentials, and thermo-pw. The dependent variable is the solar cell application of Ge-halide perovskite, while the software used is the intervening variable. It was hypothesized that the stated variables would influence the solar cell performance of Ge- and Si-halide perovskite. This general hypothesis guided this study. The properties were obtained by calculating total energies and lattice parameters, studying band structures, elastic constants, and absorption efficiencies.

CHAPTER THREE

RESEARCH METHODOLOGY

3.1 Introduction

In this chapter, an overview of the methods used in performing this research is provided. The chapter provides the theory behind Density Functional Theory, and the procedure used to obtain the results is discussed. Computational modeling describes the properties of matter based on equations. Computer simulation is performed by running programs implemented in the Quantum Espresso and SIESTA codes. The device structure used for the simulation and optimization is described.

3.2 Description of the Working of Quantum ESPRESSO and Siesta Codes

Quantum ESPRESSO is software for first-principles calculations and modeling, written in Fortran. It consists of Theory (DFT), basis sets, and pseudopotentials. The plane-wave DFT function of QE was provided by the plane-wave self-consistent field (PWscf). These PWscf were used to solve the self-consistent Kohn-Sham equations, perform total-energy calculations, and enable post-processing for data analysis and plotting. QE calculates the ground-state energy and one-electron Kohn-Sham orbitals to determine atomic forces, stresses, and structural optimization. Input cards are specific to the software code and are used to provide the required input data. The data runs programs scf, nscf, and bands to obtain the band structure and optimize the K points, Cutoff energy, and Symmetry points. The PWscf modules supported by the software include pw.x for input data and pp.x for post-processing.

The codes for data post-processing (PP) in pp.x extract the specified data from files produced by pw.x and prepare the data for plotting by writing them in formats that can be read by the plotting programs bands.x, plotband.x and dos.x. The bands.x files produced by pw.x were essential for band-structure plotting. While plotband.x read the output of bands.x and produced band-structure plots, dos.x calculated the electronic Density of States (DOS).

Siesta is one of the Max Center of Excellence's codes. It uses the standard Kohn-Sham self-consistent density-functional method with the Local density or Generalized Gradient approximations. It employs norm-conserving pseudopotentials in their fully nonlocal forms. It also employs atomic orbitals with finite support as a basis set, allowing for unlimited multiple zeta valence, angular momentum, polarization, and off-site orbitals. In its simulation, the code projects the electron wavefunctions and density onto a real-space grid to calculate the Hartree and exchange-correlation potentials and their matrix elements.

3.3 Structural and Electronic Properties of Ge and Si Perovskites

All density functional theory (DFT) calculations were performed using the respective Perdew-Burke-Ernzerhof (PBE) norm-conserving pseudopotentials. The PBE pseudopotentials for Ge and Si, distributed within the QUANTUM ESPRESSO, were used for all possible calculations. The cell shape and atomic positions were relaxed in DFT, using the standard PBE version of the GGA electron exchange-correlation functional. The structural optimization was achieved by performing a variable-cell relaxation, as implemented in Quantum Espresso, for self-consistent fields. A structural optimization of non-self-consistent fields for band-structure calculation was also performed, with the atomic positions in the input file not varied. Electronic structure calculations were performed using the desired K-mesh, which yields the density-of-states calculation.

3.4 Optoelectronic Properties of Germanium Halides

The functional GGA+U approximation was employed, and the optimization of parameter convergence was used to determine how cations influence the band gap and, consequently, the overall optical behavior of germanium-based halides. The properties to be simulated may include their ionization potentials and the behavior of their electrons.

3.5 Optoelectronic Properties of Silicon Perovskites

The essential optoelectronic properties of semiconductors that may be computed include light absorption and emission strengths, ionization potentials, and electron affinities (Merdasa, 2016). The hybrid functional GGA+U approximation was considered, and thus the optimization of convergence parameters was performed to assess how significantly the collective alignment of cations present influenced the positioning of the band gaps and, hence, the changes in the optical properties of silicon halides.

3.6 Mechanical Properties of Germanium Perovskites

The mechanical properties of $CsGeBr_3$ were used to analyze strain, stress, fracture mechanics, and deformation of solid absorber layers when these materials are used as solar cell materials. This was investigated by the stress-strain method based on the first-principles calculations. The elastic constants were obtained by calculating the total energy by displacing ions from the ground state as a function of appropriate lattice deformation. The elastic strain energy was obtained by calculating the full elastic constants, which facilitate the complete mapping of Young’s and shear moduli and Poisson’s ratios across all crystallographic orientations, to assess their anisotropy.

3.7 Governing Equations and Theorems in DFT

The simulation was based on the Density functional theorem, Born Oppenheimer approximations, Hohenberg and Kohn theorems, and the Kohn-Sham equations, which lead to the solution of the Schrödinger equation. The initial step was the direct application of density functional theory (DFT) to the calculation of many-body systems. The system provides a framework for understanding the collective behavior of a large number of interacting particles. DFT is based on the Hohenberg-Kohn (1964) theorem, which implies that all ground-state properties of an inhomogeneous electron gas can be described by a functional of the electron density. Kohn and Sham (1965) state that this one-to-one mapping holds both for an interacting and a non-interacting system, yielding the same ground-state density as the interacting system.

3.7.1 Understanding the Many-Body Problem

The time-independent Schrödinger equation has been widely used in many studies to investigate the ground-state properties of materials (Rubio, 2020). For a single particle in a 1-D field, the equation is given as;

$$\frac{\hbar^2}{2m} + \mu(x)\mu(x) = E\mu(x) \qquad \ldots\ldots\ldots\ldots\ldots\ldots(2)$$

above is easy to solve. However, when considering a system of many bodies in 3-D space, the Hamiltonian takes the form below:

$$H = \hbar^2/_{2me} \sum \nabla^2 + \frac{1}{2} \sum j \frac{ZiZje}{Ri - Rj} - \frac{\hbar^2}{2Mi} \sum{}_i \nabla \frac{1}{2} \sum{}_i j \frac{e^2}{ri - rj} - \sum \frac{r_i}{R_1} \qquad \ldots (3)$$

In **equation (3)**, the first term represents the Kinetic energy of the system, the second term represents the electron-electron potential interaction, and the last term represents the electron-nucleus interaction. In many-body systems, the number of particles complicates Schrödinger’s equation. Hence, several approximations have to be made. These are explained as follows.

3.7.2 The Born-Oppenheimer Approximation

The initial step in reducing the complexity of the Hamiltonian above is to solve the interaction between the nucleus and the electrons in the many-body system. The Born-Oppenheimer Approximation decouples the kinetic energy of the nucleus and the electrons by neglecting the kinetic energy of the nucleus and electrons tightly held to the core of the atom. The approximation then treats the electrons loosely bound to the atom's core as the main contributors to the kinetic energy of the many-body problem (Born and Huang, 1954). The Hamiltonian equation above reduces to:

$$H = \frac{\hbar^2}{2m_e}\sum_i^j \nabla^2_{i_2} + \frac{1}{2}\sum_j^i \frac{e^2}{r_i - r_j} - \sum_j^i Ze^2 \big/ r_i - R1 \qquad \text{... (4)}$$

The second term represents the electron-electron interaction, while the K.E. of the electron gas is represented by the right-hand side. The third term represents the system's interactions between the ions and electrons.

3.7.3 Hartree Approximation

This approximation uses a product of the orthonormal molecular orbits of the systems to approximate the overall wave function of the systems. According to this theory, every electron moves independently within its own orbit (Fredkin and Werthamer, 1965). However, in terms of electron interchange, it does not meet Pauli's exclusion criterion of antisymmetric wave functions (Slater, 1930).

3.7.4 The Hartree-Fock Approximation

In this approximation, anti-symmetry could be achieved by adding and subtracting all possible permutations of the Hartree product, resulting in the Hartree-Fock wave function. The resulting wave function was proven to be a determinant of a matrix (Fischer, 1977) and was called the Slater Determinant. The H-F theory showed that the wave function of the many-body system could be expressed by a single Slater determinant of N spin-orbitals expressed as:

$$\psi(1.........N) = \frac{1}{\sqrt{N!}}\left|\begin{array}{l} \psi_1(1).\psi_1(x2)............\psi 1(xN) \\ \psi_2(x1).\psi_2(x2)..........\psi 2(xN) \\ . \\ . \\ \psi_N(x1).\psi_N(x2)........\psi N(xN) \end{array}\right. \qquad \ldots (5)$$

In the expression above, the variable x1... captured the coordinates of space and spin of the electrons. In this representation, the wave function ψ is known to capture sufficient physics to provide solutions to the Hamiltonian. Finally, the new wave function is anti-symmetric, in accordance with Pauli's exclusion principle. When applied to the Hamiltonian, the Hartree-Fock methodology reduces the Hamiltonian to the form:

$$2\nabla^2\psi i(r) + V_{ion}(r)\psi i(r) + U\psi i(r) = \text{€} i\psi i(r) \qquad \ldots (6)$$

This approach fails when it comes to making quantitative predictions.

3.7.5 Density Functional Theory

This is a computational approach applied in materials science and physics to explain the dynamics of electrons at the fundamental level (Sholl and Steckel, 2011). The DFT approach solves the fundamental problem of Schrödinger's equation for a many-body problem. The Kohn-Sham equation is used to implement DFT calculations.

3.7.6 Hohenberg and Kohn Theorems

Hohenberg and Kohn formulated the following two theorems to explain the basics of DFT. The first theorem states that for a given system of interacting particles in an external potential, the potential from external fields given by V_{ext} and subsequently the total energy of the system is a unique functional of the ground state electron density given by $n_0(r)$. From this theorem, it can be inferred that all properties of the system being investigated can be determined from the ground-state electron density based on the fact that the external potential of the system dictates the Hamiltonian from which the wave function of the system being investigated can be inferred (Hohenberg and Kohn, 1964).

The second theorem states that the precise ground-state energy of a system is given by the minimum value of an overall functional. The theorem also states that the density that actually minimizes the given functional is the true ground-state density of the system, $n_0(r)$ (Hohenberg and Kohn, 1964).

A mathematical relationship for the functional being explained in the theorem is shown below:

$$E[n(r)] = F_{HK}[n(r)] + \int_i^j \quad V(r)n(r)d^3r \qquad \ldots\ (7)$$

In many-body systems, the function is unknown. However, in single-electron systems, the functional is expressed as follows:

$$E[\psi_i] = E_{known}(\psi_i) + E_{xc}(\psi_i) \qquad \ldots\ (8)$$

3.7.7 Kohn and Sham Equations

Having broken down the functional into **equation 8** above, Kohn and Sham formulated a set of equations to identify the electron density that minimizes the functional (Kohn and Sham, 1965). These equations are commonly known as the Kohn-Sham equations and are represented as follows:

$$[-\frac{\hbar^2}{2m}\nabla^2 + V(r) + \dot{V}(r) + V(xc)]\varphi_i(r) = \varepsilon_i\psi_i(r) \qquad \ldots\ (9)$$

3.7.8 Exchange Correlation Functionals

This approach is based on the uniform gas theorem, in which the electron density is assumed to be uniform throughout the system (Sholl and Steckel, 2011). Evidently, this approach is incorrect, since in most materials the electron density varies significantly due to chemical bonding. In the uniform electron gas approach, the exchange-correlation potential in the K-S equation is given as the potential observed at a given arbitrary point in the electron density (Sholl and Steckel, 2011). Thus, the exchange correlation potential can be explained as:

$$V_H(r) = e^2 \int_i^j \frac{n(r')}{r-r'} d^3r' = \epsilon_i \psi_i(r) \qquad \dots (10)$$

Equation 10 is referred to as the Local Density Approximation, LDA. This approach tends to be ineffective since it does not provide the actual exchange-correlation functional.

3.8 Generalized Gradient Approximation (GGA)

This method is a continuation of LDA, taking into account both the density of the uniform electron gas and its deviation from homogeneity by considering the gradient of the charge density. However, LDA and GGA both have limitations when describing the correct electronic properties of some materials, for instance, transition-metal oxides and strongly correlated systems.

3.9 Pseudopotentials

This has been used to reduce the computational complexity of DFT calculations (Cohen, 1997). Pseudopotential can be considered to be a replacement of the core electrons of the system with a defined density that is consistent with most of the physical and structural properties of the actual electron core. An important property of a pseudopotential is its transferability. Transferability refers to the ability of a pseudopotential to be placed in a new environment different from the one in which it was created without being modified in any major way. Pseudopotentials can be broadly categorized into hard pseudopotentials if the required cutoff energies are high or soft pseudopotentials if the required cutoff energies are low (Troullier and Martins, 1990).

3.10 Self-Consistent Iterative Solution

Density Functional Theory is a method used to describe a system with the use of electron density. DFT is used to predict and analyze the electronic and optical properties of materials, where the electronic density distribution n(r) is considered. Currently, DFT is applied in many first-principles or ab initio codes. The sequence scheme for the calculation of material properties can be generalized as shown in the Figure 5 below.

Figure 5

Schematic Flow of the solution of the Schrödinger Equation to obtain a self-consistent Electron density

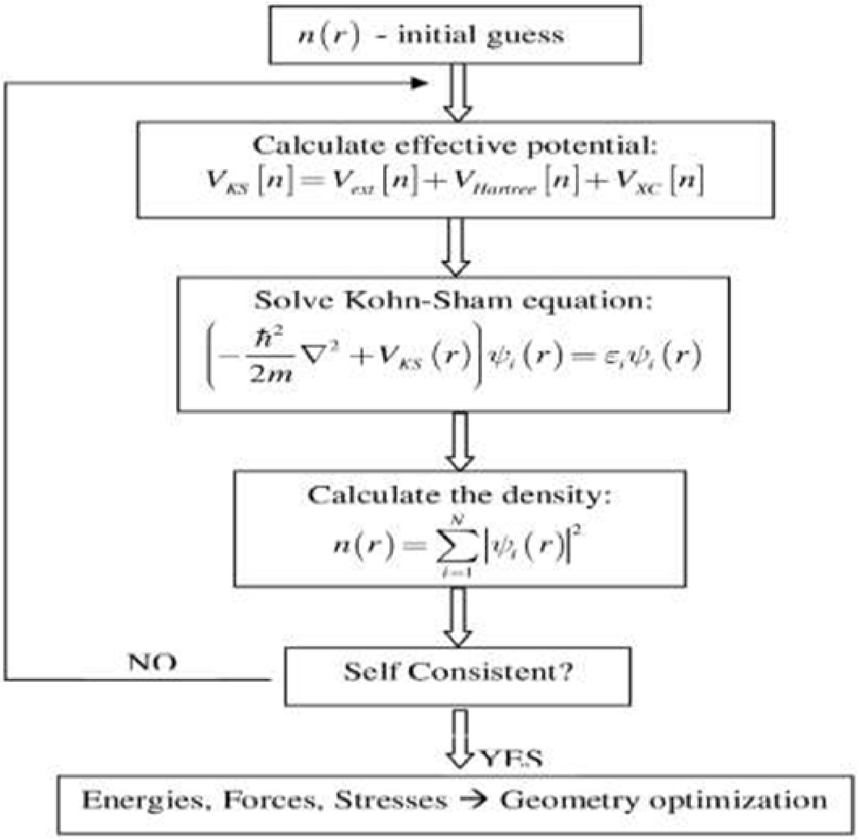

3.11 Implementation

The simulations were performed on CsXBr3 (X=Si, Ge) using density functional theory (Hohenberg and Kohn, 1964; Kohn and Sham, 1965) as implemented in the Quantum Espresso code (Soler et al., 2002).In the calculations, we replaced the core electrons with ab initio norm-conserving fully separable (Kleinman and Bylander, 1982) and Troullier-Martin pseudopotentials (Troullier and Martins, 1991). A Fermi-Dirac smearing distribution with energy of 0.075 eV was used to smear the occupancy of the one-particle electronic eigenstates. First, to relax the atomic structure and the one particle density matrix with a sensible number of k-points 17×17×17 Monkhorst-Pack (Monkhorst and Pack,1976) and secondly, freezing the relaxed structure and density matrix, a non-self-consistent band structure calculation was performed with a much denser sampling of 60×60×60 in the real space integrations, a uniform grid with an equivalent plane-wave cutoff of 400Ry was used.

3.12 The Brillouin Zone (Reciprocal Space) and K-Points

Density Functional Theory is used in materials research for calculations in a system of periodic atoms in space. A supercell is a cell with atoms repeated periodically; these supercells are identified with the lattice vectors $\mathbf{a}_1$, $\mathbf{a}_2$, and $\mathbf{a}_3$. The solutions of the Schrödinger equations for a periodic system must be in line with Bloch’s theorem. The primitive cell concept in k-space follows the Wigner-Seitz cell, where the reciprocal lattice vectors are defined in the same way as in real space. Cells in k space are referred to as the Brillouin zone, which contains several k-points with special symmetry. These points are given independent identities; one of the most important is the Gamma point (Γ point), which is the center of the reciprocal space, implying k = 0 at the Γ point (Saparov and Mitzi, 2016).

3.13 Elastic Constants

The elastic constants for the cubic and tetragonal phases of CsGeBr3 and CsSiBr3 were determined by accurate structural relaxation of the materials to an approximately zero-stress state. Subsequently, perturbations are applied to the lattice vectors, and the resulting stress tensor is calculated, allowing relaxation of the ionic degrees of freedom. The constitutive relations from linear elasticity, which relate stress and strain, are finally employed to fit the full 6x6 elastic tensor.

The equilibrium bulk modulus and its pressure derivative were obtained from the Murnaghan EoS. The bulk modulus measures a material's resistance to compression. The volume and bulk modulus of materials are inversely related (Singh and Dwivedi, 2012). The bulk modulus is given by equation (11).

$$B = -V\frac{\partial P}{\partial V} \qquad \text{… (11)}$$

where V stands for volume, P for pressure, and B for bulk modulus. Equation (12) below provides the pressure.

$$P = \frac{-\partial E}{\partial V} \qquad \text{... (12)}$$

Equation (12) then reduces (11) into equation (13)

$$B = V\frac{\partial^2 E}{\partial V^2} \qquad \text{…. (13)}$$

The pressure derivative of the bulk modulus is given by;

$$B^I = \frac{\partial B}{\partial P} = \frac{1}{B}\left(V\frac{\partial}{\partial V}\left(V\frac{\partial^2 E}{\partial V^2}\right)\right) \qquad \text{… (14)}$$

Elastic properties are crucial for determining the mechanical stability of materials. The properties studied in this work are the elastic constants, the bulk, Young, and shear moduli, and Poisson’s ratio. The elastic properties were calculated using the *thermo_pw* within Q.E. Other elastic properties, such as the bulk and shear moduli, the Young’s and Poisson’s ratios, were calculated from the elastic constants. The elastic constants are denoted by C_{ij} and vary from one crystal system to another. From the Born stability criteria (Mouhat and Coudert, 2014), these elastic constants need to meet certain conditions and be positive for the materials to be considered mechanically stable. In the cubic phase, the necessary conditions are given by equations (15) (Hou, 2008; Li *et al.*, 2017; Mouhat and Coudert, 2014);

$$C_{11} - C_{12} > 0, C_{11} + 2C_{12} > 0, \quad C_{44} > \qquad \ldots\ldots\ldots \qquad \ldots(15)$$

A tetragonal material is regarded as mechanically stable if **equations (15)** are met (Dong *et al.*, 2013; Mouhat and Coudert, 2014);

$$C_{11} > |C_{12}|, 2C_{13}^2 < C_{33}(C_{11} + C_{12}) \qquad \ldots\ldots\ldots\ldots\ldots\ldots\ldots\ldots\ldots (16)$$

Following the computation of the elastic constants, the moduli are computed using the Reuss and Voigt theories, with the Hill averaging scheme used to obtain the average (Hill, 1932). Equations (18) and (19), respectively, provide the bulk and shear G_V moduli of the cubic phase based on the Cij's and the Voigt theory (Dong *et al.*, 2013).

$$B_V = \frac{1}{9}[(C_{11} + C_{22} + C_{33}) + 2(C_{12} + C_{23} + C_{31})] \qquad \ldots.\ (17)$$

$$G_V = \frac{1}{15}[(C_{11} + C_{22} + C_{33}) - (C_{12} + C_{23} + C_{31}) + 3(C_{44} + C_{55} + C_{66})] \qquad \ldots\ (18)$$

Equations (19) and **(20)** can be used to derive the bulk B_R and shear moduli from the elastic constants in the Reuss theory.

$$\frac{1}{B_R} = (S_{11} + S_{22} + S_{33}) + 2(S_{12} + S_{23} + S_{31}) \qquad \ldots\ (19)$$

$$\frac{15}{G_R} = 4(S_{11} + S_{22} + S_{33}) - 4(S_{12} + S_{23} + S_{31}) + 3(S_{44} + S_{55} + S_{66}) \qquad \ldots\ (20)$$

The elastic compliances are the S_{ij}. The elastic compliances inversely represent the matrix of elastic constants. According to the Hill averaging system, the averages of the two theories or equations (21) and (22) provide the bulk BH and shear GH moduli, respectively.

$$B_H = \frac{B_V + B_R}{2} \qquad \ldots (21)$$

$$G_H = \frac{G_V + G_R}{2} \qquad \ldots (22)$$

The Pugh method (Dong *et al*., 2013; Pugh, 1954) can be used to determine a material's ductility or brittleness by examining the relationship between B/G and the crucial value of 1.75. The material is deemed ductile if the ratio B/G is above this value, and vice versa.

Equations (23) and (24) can be used to obtain the Young's modulus and the Poisson's ratio from the shear and bulk moduli, respectively, after the elastic constants and moduli have been calculated (Dong *et al*., 2013; Hou, 2008).

$$v = \frac{3B_H - 2G_H}{2(3B_H + G_H)} \qquad \ldots \quad (23)$$

$$E_H = \frac{9B_H G_H}{(3B_H + G_H)} \qquad \ldots (24)$$

The cubic phase perovskites satisfy the Born stability criterion and are therefore mechanically and elastically stable. The monoclinic structures are mechanically unstable because the elastic constants are negative and do not satisfy the Born stability criteria. To the best of our knowledge, there is no previous work reported in the literature; hence, we could not compare mechanical properties.

3.14 Optical Properties

The study of optical properties is crucial in solar cells, as it explains how a material interacts with light. To study the optical properties, the complex dielectric function is investigated. This function is dependent on the electronic band structure of the given material and affects its properties. From the dielectric function, the other optical properties of the material, such as the refractive index, reflectivity, absorption coefficient, and extinction index, can be obtained. The dielectric function is made up of the real and imaginary parts and is given by equation (25).

$$E = \varepsilon_1(\omega) + i\varepsilon_2(\omega) \qquad \dots (25)$$

where $\varepsilon_2(\omega)$ is the imaginary part and $\varepsilon_1(\omega)$ is the real part. The Kramers-Kronig relation can be used to obtain R(ω) once the imaginary part has been determined.

$$R(\omega) = \frac{n+iK-1}{n+iK+1} \qquad \dots (26)$$

where $R(\omega)$ is the reflectivity, and $n(\omega)$ is the refractive index. $K(\omega)$ is the extinction index.

The coefficient of optical absorption $\alpha(\omega)$ is

$$\alpha(\omega) = \sqrt{2}\omega\left(\sqrt{\varepsilon_1^2(\omega) + \varepsilon_2^2(\omega)} - \varepsilon_1(\omega)\right)^{\frac{1}{2}}$$

The refractive index $n(\omega)$is

$$n(\omega) = \left(\frac{\sqrt{\varepsilon_1^2(\omega)+\varepsilon_2^2(\omega)}+\varepsilon_1(\omega)}{2}\right)^{\frac{1}{2}} \qquad \dots (28)$$

the reflectivity $R(\omega)$

$$R(\omega) = \frac{(n-1)^2+K^2}{(n+1)^2+K^2} \qquad \dots (29)$$

the exciton index $K(\omega)$ as in equation (30)

$$K(\omega) = \left(\frac{\sqrt{\varepsilon_1^2(\omega) + \varepsilon_2^2(\omega)} - \varepsilon_1(\omega)}{2} \right)^{\frac{1}{2}} \quad \ldots (30)$$

Equation (31) provides the energy loss, the amount of energy lost due to radiation, absorption, scattering, and other processes.

$$L(\omega) = \frac{\varepsilon_2(\omega)}{\varepsilon_1^2(\omega) + \varepsilon_2^2(\omega)} \quad \ldots (31)$$

CHAPTER FOUR

RESULTS AND DISCUSSIONS

4.1. Introduction

This chapter discusses the results, data on the cubic, monoclinic, and tetragonal phases, structural properties, electronic, elastic, and dielectric constants, and the solar cell applications of CsSiBr3 and CsGeBr3 perovskites. It compares the results from this work with other first-principles research on perovskite materials and other works. In this work, the structural, electronic, elastic, and optical properties of $CsGeBr_3$ and $CsSiBr_3$ have been calculated using density functional theory as implemented in the QUANTUM ESPRESSO computer code (Giannozzi *et al.*, 2009). It uses the pseudopotential approach, which allows it to calculate many material properties. It is multi-purpose, multi-platform software for *ab-initio* calculation of periodic and non-periodic condensed matter (Perdew *et al.*, 1981). Ion-electron interactions are described using Ultrasoft pseudopotentials. To sample the Brillouin zone, k-mesh point densities were used according to the Monkhorst-Pack scheme (Monkhorst *et al.*, 1976). To calculate the ground-state density, Quantum ESPRESSO uses a self-consistent cycle to solve the Kohn-Sham functionals.

4.2 Phases of $CsSiBr_3$ and $CsGeBr_3$ and Solar Cell Application

An analysis of cubic, monoclinic, and tetragonal phases of $CsSiBr_3$ and $CsGeBr_3$ was done. The original structures from the database and the optimized structures were simulated using the same values for ecutwfc and ecutrho, and the structures were visualized before and after optimization using XcrySDen (Kokalj, 1999). At the initial stage, the structural optimizations for both halide perovskite compounds, CsGeBr3 and CsSiBr3, were performed using the GGA-PBE method. Then, we extracted equilibrium results for structural parameters such as ground-state energy ($E0$), unit-cell volume ($V0$), lattice constants ($a0$), bulk modulus (B), and the first pressure derivative of the bulk modulus$B$ (B'). Both of these results of $CsGeBr_3$ and $CsSiBr_3$ are expected by fitting the variation of the total energy (E) per unit cell as a function of the corresponding unit cell volume (V). The findings reveal that the cubic phase of both $CsGeBr_3$ and $CsSiBr_3$ at and above room temperature was more stable compared to the tetragonal and monoclinic phases, as depicted in the Energy-Volume curve in Figure 6 below.

Figure 6

Energy against Volume Curve for the Monoclinic, Cubic and Tetragonal phases of $CsGeBr_3$

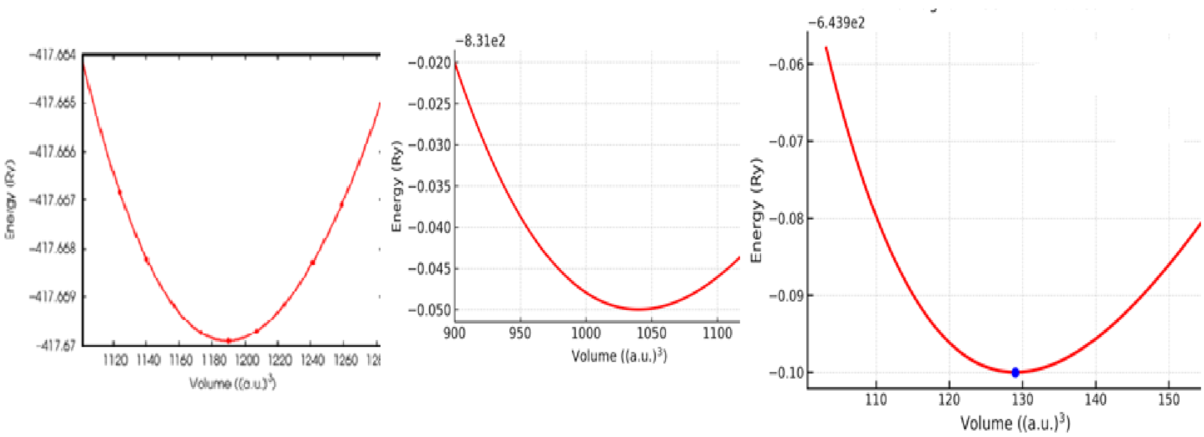

Figure 7

Energy against Volume Curve for the Cubic, Monoclinic, and Tetragonal phases of $CsSiBr_3$

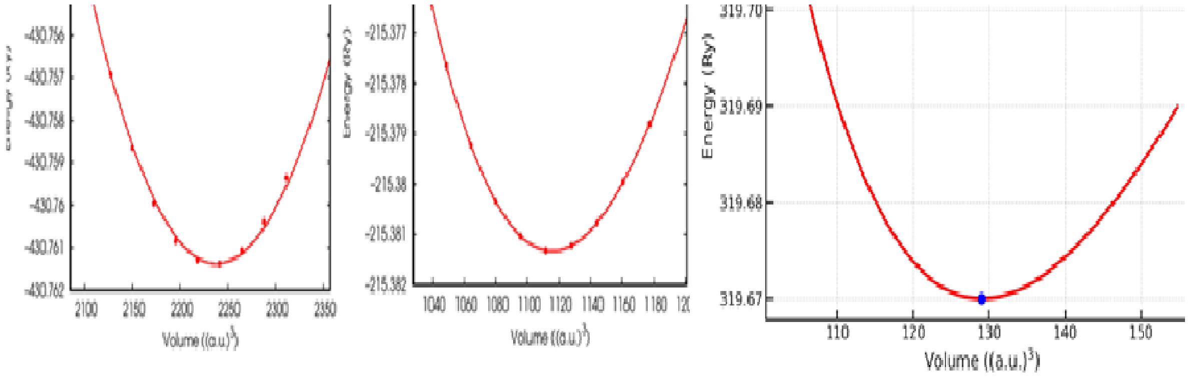

From Figure 6, the cubic phase of CsGeBr3 showed the lowest energy of -831.9 Ry at 1040 (a.u)3, the monoclinic phase showed -417.669 Ry at around 1180 (a.u)3, and the tetragonal phase gave −644.0 Ry at 129.0 (a.u) 3 of the equilibrium volume. The absolute minimum total energy determines stability. Hence, the cubic phase was more stable. From Figure 7, the cubic phase of CsSiBr3 gave -430.760 Ry at 2240 (a.u) ^{3}; in the monoclinic phase, the energy obtained was -215.381 Ry at 1120 (a.u) ^{3}; and the tetragonal phase gave 319.67 Ry at 129.0 (a.u)^3. Stability in this analysis was determined by selecting the lowest point on the energy (Ry) versus volume (a.u)3 curve. The curves for the cubic phases indicated stability, with energy increasing on either side of Vo due to compression or expansion. Hence, the cubic phases for both CsGeBr3 and CsSiBr3 were concluded to be stable compared to the monoclinic and tetragonal phases at very high temperatures.

4.2.1 Lattice Parameters

The lattice parameters obtained were a = 8.505 Å, b = 9.232 Å, and c = 15.04 Å. Murnaghan's equation of state was used according to Madsen *et al*. (2016) to optimize volume by minimizing the total energy with respect to volume. The relationship between the energy and volume of the three phases of the perovskite cell is represented by the energy-volume diagrams (6 and 7) above.

The lattice constants for $CsSiBr_3$ and $CsGeBr_3$ were calculated to be 5.89 Å and 5.75 Å, respectively, and showed good agreement with previously calculated results. Table 1 below provides a summary of the grid constants for the cubic phase of $CsGeBr_3$ and $CsSiBr_3$.

Table 1

Number of Bonds, the Bond length of Chemical bonding of Cs-Br/Ge-Br and the lattice constant of the cubic phase of $CsGeBr_3$ and $CsSiBr_3$ Compounds.

Point group (O_h)	atom-atom	number of bonds	bond length(Å)	Lattice Constant(Å)
$CsGeBr_3$	Cs-Br	12	4.09	5.75
	Ge-Br	6	3.20	5.76
$CsSiBr_3$	Cs-Br	12	4.30	5.89
	Si-Br	6	2.79	5.87

Table 1 illustrates the achiral octahedral symmetry point group, O_h. This group has the same rotation axes as O, but with mirror planes T_d and T_h. The bond length depicts the average distance between nuclei of two bonded atoms in either the $CsGeBr_3$ or $CsSiBr_3$ molecule. The lattice constant is simply the geometric constant that measures the distance between the atoms in this crystal structure. The values for bond length and lattice constants in both crystals are not the same because they exhibit body-centered cubic structures.

4.3 Electronic Properties

4.3.1 Electronic Properties of the Cubic Structures of $CsGeBr_3$ and $CsSiBr_3$

The band gap of the material is a crucial tenet that determines the efficiency of a solar cell. Semiconducting materials with suitable band gaps are crucial for the fabrication of solar cells. As the majority of the Sun's radiation that reaches the surface of the Earth has energy <2 eV, solar cell materials with band gaps greater than 2 eV and lower than 0.9 eV are less effective. In addition, materials with a band gap of 0.9–2.0 eV are effective not only for single-junction SCs but also for the top and bottom cells in the tandem structure (Ming et al., 2023). To probe the electronic properties, we have calculated the band structures along paths connecting the high symmetry points Γ(0 0 0), X(0.5 0.0 0.0), M(0.5 0.5 0.0), R(0.5 0.5 0.5), and Γ(0 0 0) for the Si-based; and Γ(0 0 0), Z(0.5 0.5 0.5), F(0.5 0.5 0.0), and Γ(0 0 0) for the cubic phase of Ge-based compounds

Figure 8

Electonic Band Structure for for the Cubic Phase of CsGeBR3

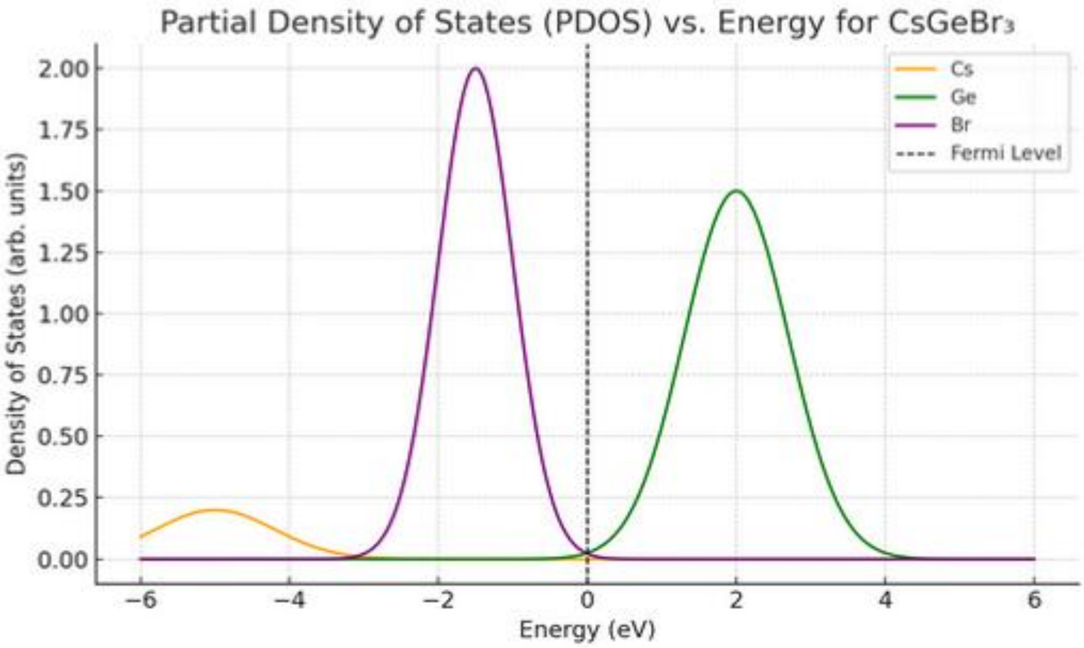

Figure 9

Partial Density of State for the Cubic Phase of $CsGeBr_3$

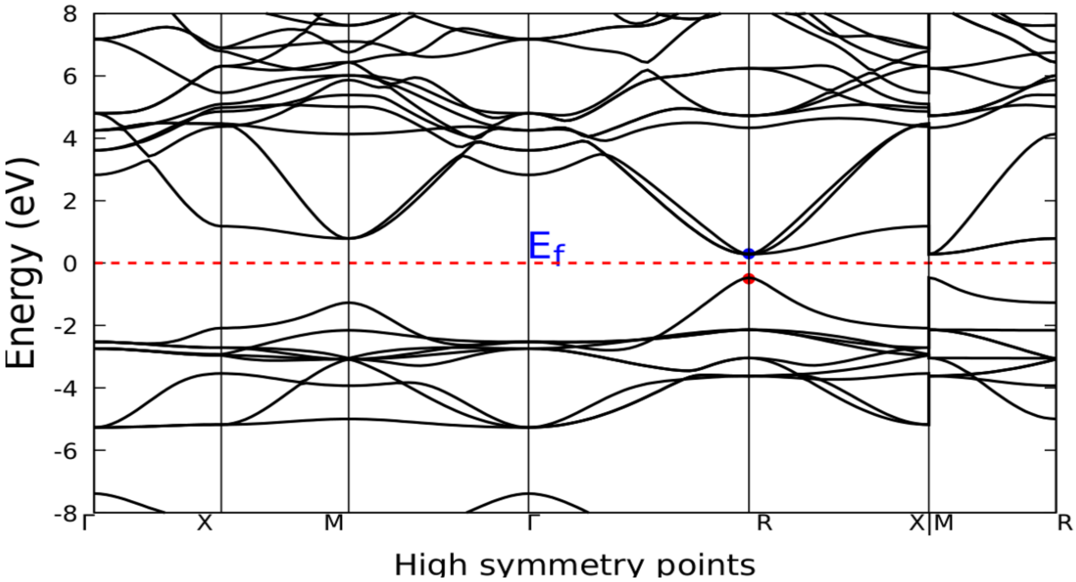

As illustrated in Figures 8 and 9, the cubic phase of the material CsGeBr3 exhibits a direct band gap, with the valence band maximum (VBM) and conduction band minimum (CBM) located at R for germanium-based perovskites. The band gap for CsGeBr3 is 0.7 eV at the R point, as depicted in Figures 8 and 9. These band gap value is considerably lower than experimental findings, suggesting that the PBE functional tends to underestimate band gaps in most cases, except a few lead-based halide perovskites (Ali *et al.*, 2020; Zhu *et al.*, 2019).

To investigate the influence of spin-orbit coupling (SOC), we employed PBE to evaluate band gaps with SOC included. It was found that the band gaps for all compositions decreased under SOC (PBE+SOC) due to the separation and downward shift of the CBM (Qian *et al.*, 2016). Additionally, the SOC values for germanium halides (0.04 eV - 0.06 eV) are notably lower than those for silicon halides (0.36 eV - 0.37 eV). The electronic properties of hybrid halide perovskites are of great importance and need to be studied, as these materials are potential light-harvesting materials. We employed PBE-GGA exchange-correlation potentials to study various electronic properties, including electron density plots, band structures, and energy band gaps. The band structure and the density of states (DOS) are important in analyzing the electronic properties of a material.

The calculated band structure of the cubic phase of $CsSiBr_3$ crystal along the high-symmetry lines in the first Brillouin zone is presented in Figure 10 below.

Figure 10

Electronic band structure and Partial Density of State for the Cubic Phase of $CsSiBr_3$

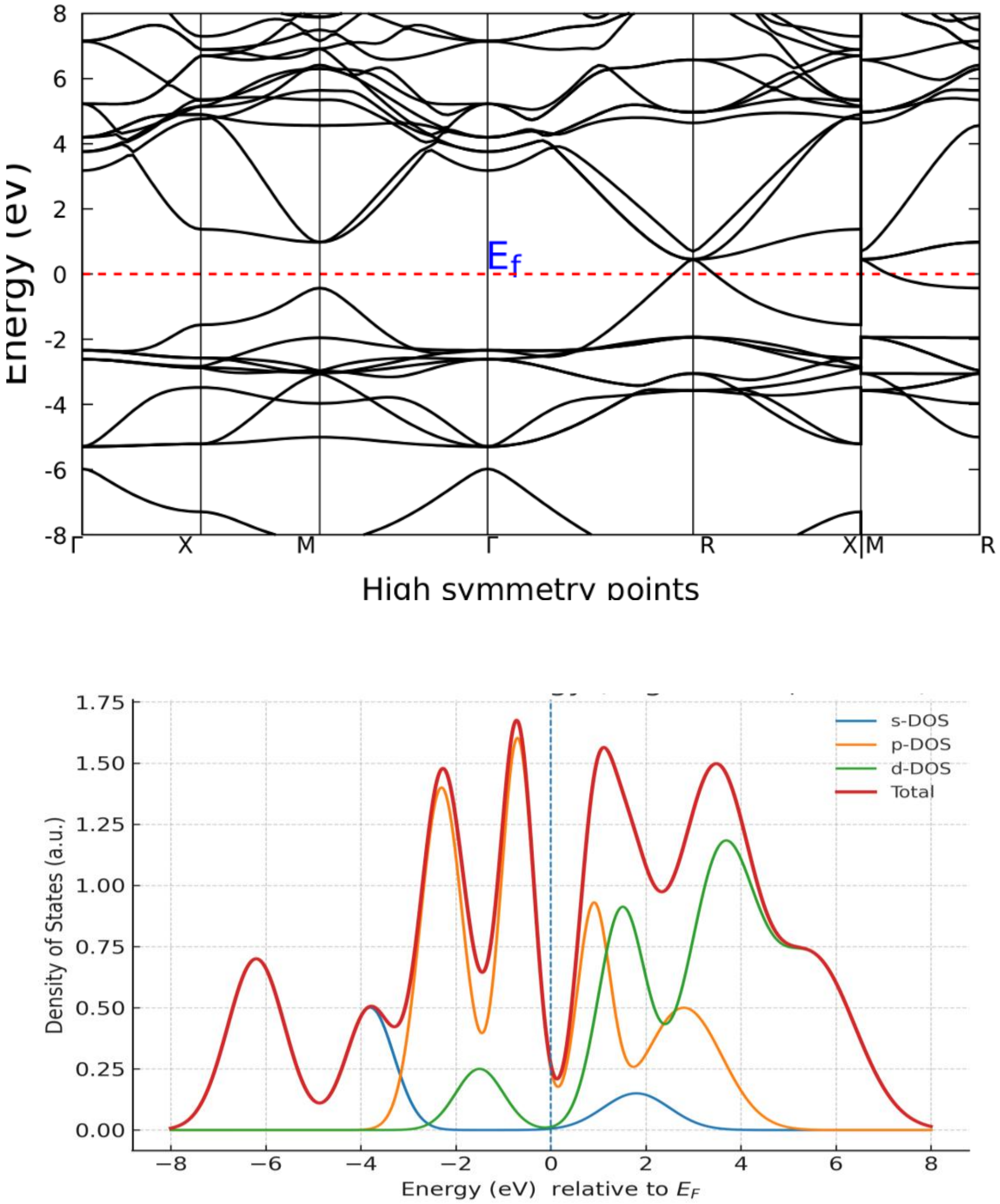

the cubic crystal of $CsSiBr_3$ has a narrow band gap at the gamma symmetry points, with a 0.29 eV band gap energy calculated using DFT exchange–correlation functionals. From Figure 10, there is a sharp rise just below E_F, then a strong onset above E_F. This showed a tiny gap of 0.01 eV, suggesting that CsSiBr3 is either metallic or has a small band gap at the chosen threshold.

From figures 8, 9, and 10, it is observed that CsGeBr3 and CsSiBr3 have direct band gaps of 0.7 eV and 0.01 eV, which are comparable to the values of 0.834 eV and 0.099 eV reported by Jain et al. (2011). The values are reasonable, since it is known that DFT usually underestimates the band gap, while HSE06 provides a more accurate value. However, this narrow band gap of CsSiBr$_3$ could be utilized in solar cells, potentially absorbing a portion of the infrared spectrum that larger band gaps might lack.

4.4 Elastic Properties

4.4.1 Elastic Properties of CsGeBr$_3$ and CsSiBr$_3$

The table below shows the elastic properties of the Cubic, Tetragonal, and monoclinic phases of CsGeBr$_3$ and CsSiBr$_3$.

Table 2

The calculated elastic constants (C_{ij}) in (GPa)

Material	C_{11}	C_{12}	C_{13}	C_{22}	C_{23}	C_{44}	C_{33}	C_{55}	C_{66}
Ge Cubic	46.866	10.184				9.624			
Si Cubic	47.726	12.325				12.126			
Ge Tetragonal	41.246	21.301	10.486	41.12246	10.486	38.908	9.372	9.372	9.372
Si Tetragonal	44.894	19.376	11.813	44.894	1.813	39.597	11.683	11.683	11.683
Ge Monoclinic	43.718	20.416	12.684	43.173	10.678	39.809	10.684	10.237	10.412
Si Monoclinic	44.194	16.345	14.318	45.498	10.103	28.795	12.386	12.668	12.814

C_{11}, C_{12}, and C_{44} are three elastic constants that characterize cubic crystals. They are used to describe the relationship between stress and strain in a material. C_{11} describes the uniaxial elastic response of a cubic structure, C_{12} characterizes the elastic properties of a cubic structure, and C_{44} describes the relationship between strain and stress in a cubic structure.

The bulk and shear moduli in the Voigt and Reuss approximations, along with their averages in GPa, are shown in Table 3 below. The B_V, ,G_V , B_R , G_R, B_H, G_H are obtained from equations (42) and (43) respectively. The cubic structures had the lowest bulk moduli, with the germanium compounds having lower moduli than their silicon counterparts. We also noted that the monoclinic structures had inconsistent figures of both the moduli and elastic constants, showing that they are highly elastically unstable.

Table 3

The bulk (B_V, B_R, B_H) and shear (G_V, G_R, G_H) moduli in N/m^2

Material	B_V	B_R	B_H	G_V	G_V	G_H
Ge Cubic	22.411	22.411	22.411	13.111	11.883	12.497
Si Cubic	24.126	24.126	24.126	14.356	13.874	14.115
Ge Tetragonal	22.883	22.720	22.802	13.002	11.755	12.378
Si Tetragonal	23.932	23.800	23.866	14.237	13.700	13.969
Ge Monoclin	23.686	23.739	23.497	15.383	14.141	14.749
Si Monoclinic	24.612	24.502	24.208	15.141	13.793	12.973

The Pugh criterion (Pugh, 1954), which is used to determine the ductile or brittle nature of materials, was employed: a material is ductile if and brittle otherwise. The $\frac{B}{G}$ ratio obtained implies that the germanium-containing perovskites are ductile, while the silico-containing materials are brittle because their $\frac{B}{G}$ ratios are less than the critical value of 1.75. The data obtained from the Poisson ratio also agree with these findings. Using the critical value of the Poisson's ratio, 0.26, the materials containing germanium at the B site show that they are ductile in nature. The perovskite materials with silicon in the B site have $\nu < 0.26$ indicated that they are brittle, with the monoclinic structure having the lowest value, $0.074 < 0.26$ showing that it is highly brittle, higher than the cubic and tetragonal materials. From the calculations, the Pugh's criterion and the Poisson ratio are consistent in identifying the ductility of materials. This implies that germanium perovskite structures would crack easily, especially during materials engineering for applications.

Table 4

The Poisson's ratio (ν) Young's modulus E_H in GPa Pugh's ratio $\frac{B}{G}$

Material	$\frac{B}{G}$	ν	E_H
Ge Cubic	1.793	0.264	31.604
Si Cubic	1.709	0.255	35.433
Ge Tetragonal	1.842	0.270	31.536
Si Tetragonal	1.708	0.255	31.063
Ge Monoclinic	1.924	0.272	30.360
Si Monoclinic	1.915	0.263	30.460

From Table 4 above, we find that the Poisson's ratios of the $CsGeBr_3$ and $CsSiBr_3$ are sensitive to the change of bond length and angles. The smallest value of Young's modulus is 31.604 GPa (along the [1 0 0] directions) and the greatest is 35.433 GPa (along the [1 1 1] directions) for the cubic phase of $CsGeBr_3$ and $CsSiBr_3$, respectively. These values, however, vary with crystal orientation. They also show that these materials can withstand external stresses, such as wind and moisture. The cubic phases of CsGeBr3 and CsSiBr3 exhibited higher Young's moduli than the tetragonal and monoclinic phases; hence, they are mechanically stable, a tenet essential for long-term device performance.

4.5 Optical Properties of $CsGeBr_3$ and $CsSiBr_3$ for Solar Cell Application

The real part $\varepsilon_1(\omega)$ and imaginary part ε_2 (ω) were calculated using *thermo_pw*, a Quantum ESPRESSO package. The results were obtained as shown in Figure 11 below;

Figure 11

Relationship between Real part and imaginary part against Energy in eV of $CsGeBr_3$ in the Cubic Phase

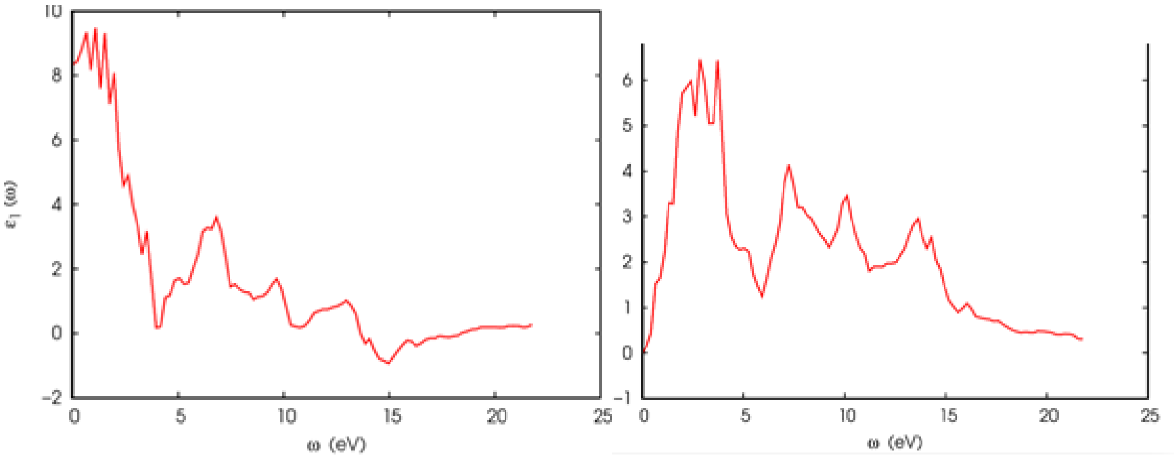

For the Real part in Figure 11, at low energy (0–2 eV), ε_1 is very high (~9–10), suggesting a strong polarization response at low photon energies. It decreases with increasing energy and oscillates around 0–4 between 2–10 eV, showing electronic interband transitions. Around 15–20 eV, ε_1 becomes negative at some points. After ~20 eV, ε_1 stabilizes near zero, showing reduced dielectric response. For the imaginary part, a strong absorption peak appears between 2 and 5 eV, with a maximum of ~6. Multiple peaks are observed at 6–12 eV, indicating several allowed transitions between the valence and conduction bands. Beyond 15 eV, absorption decreases steadily, approaching near zero above 20 eV. The analysis reveals that CsGeBr3 shows a high dielectric constant at low energies and strong optical absorption in the visible–UV range, with a band gap (Eg) of 1.8–2.0 eV. The relationship between the real and imaginary parts against the energy of $CsSiBr_3$ is depicted in the graphs below;

Figure 12

Relationship between Real and Imaginary Parts of $CsSiBr_3$ *in Cubic Phase*

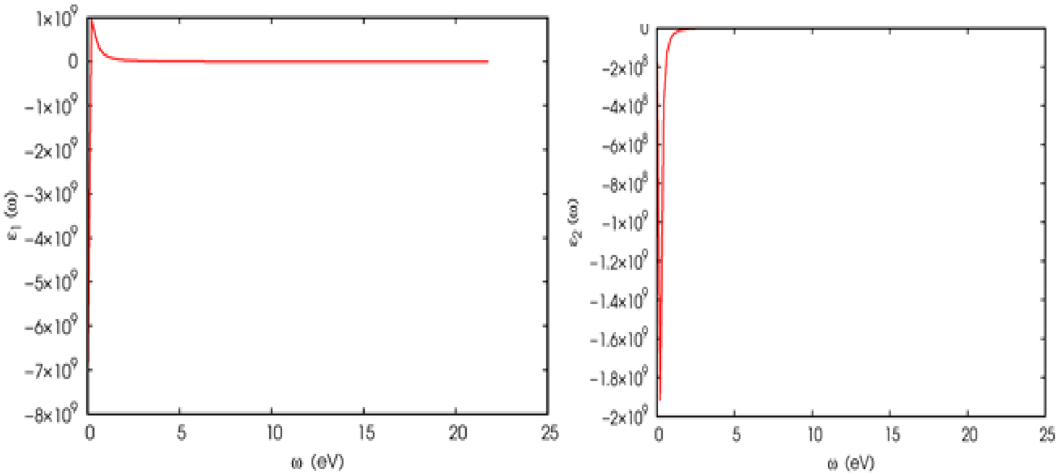

For the real part in Figure 12, $\varepsilon_1(\omega)$ starts at a very large negative value ($\sim -8\times10^9$) near $\omega \approx 0$, then rapidly increases toward zero and stabilizes around a negative constant for higher photon energies (above ~5 eV). The large negative $\varepsilon_1(\omega)$ at low energies usually suggests metallic screening behavior or a strong Drude-like free-carrier contribution. $\varepsilon_1(\omega)$ does not cross into positive values, implying that $CsSiBr_3$ does not show a conventional dielectric optical response in this range. Instead, it indicates a strong metallic nature.

For the imaginary part, $\varepsilon_2(\omega)$ is also very large and negative (starting from $\sim -2\times10^9$), and then it approaches a less negative constant value with increasing ω. $\varepsilon_2(\omega)$ indicates interband transitions, absorption edges, and energy loss. A sharp peak near low energies marked the onset of strong optical absorption. The dielectric response exhibited here is highly unusual, with both $\varepsilon_1(\omega)$ and $\varepsilon_2(\omega)$ being large negative values. This strongly suggests $CsSiBr_3$ behaves like a metallic system with a strong free-carrier contribution. Hence, $CsSiBr_3$ is not suitable for solar cell applications.

4.6 The Dielectric Constants of Germanium-Based Perovskites

The optical properties express the interaction of light with the material medium. In this study, the optical properties of $CsGeBr_3$ and $CsSiBr_3$ metal halide perovskites based on the DFT scheme of measuring the different optical parameters were studied. In the solar spectrum, the visible energy wavelength ranges from around 380-780nm, translating to approximately 1.6-3. 25eV.The humps then decrease rapidly, followed by small humps, which can be caused by inter-band transitions between the valence band and the conduction band. On the other hand, the imaginary part of the dielectric function is a measure of the extent of light absorption. High absorption peaks are observed in the visible spectral region at energies around 2.5–4.5 eV. Several weak peaks are observed in the energy range of 4.5–14 eV.

Table 5

The Zero-Frequency Values of the Real Part of the Dielectric Function and Band Gaps

Compound	ε 0 (ω)	Band gaps (eV)	References
$CsGeBr_3$	4.0	0.7	This work
$MAPbI_3$	6.0	1.7	Wang *et al* 2015
$CsSiBr_3$	5.0	1.73	Ahmad *et al* 2017

The absorption coefficient α(ω), the imaginary part of the refractive index *k*(ω), the real part of the refractive index n(ω), and the reflectivity *R*(ω) have been calculated to elucidate better the optical properties of the $CsGeBr_3$ and $CsSiBr_3$ compounds. Apparently, these compounds exhibit strong absorption and weak reflectance. The α(ω) is equal to 0, and the *R*(ω) is almost independent of the energy in the visible region, as they lack electronic excitation contributions. The rapid increase in the absorption coefficient is due to various inter-band transitions. The inverse values of the absorption coefficient are equal to 200 and 100 Å for $CsGeBr_3$ and $CsSiBr_3$, respectively. These findings imply that photons propagating through the medium are readily absorbed by the medium's rich electronic excitations.

4.7 Solar Cell Application of $CsGeBr_3$ and $CsSiBr_3$ Perovskites

Solar cell operation depends directly on the absorber's light-absorbing efficiency. The plot shows the absorption spectrum over 130–800 nm, which spans a large portion of the solar spectrum. In Figure 13, the equivalent plots as a function of energy are presented.

Figure 13

Relationship between absorption against energy of $CsGeBr_3$ and $CsSiBr_3$ in Cubic, Tetragonal, and Monoclinic Phases

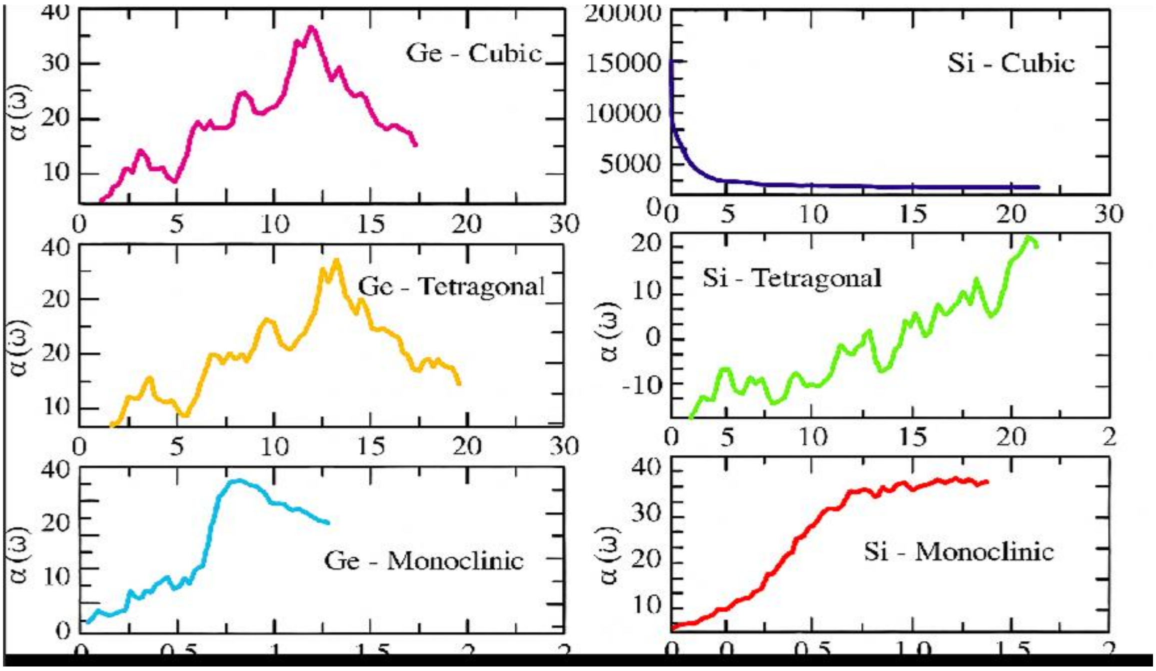

From Figure 13, germanium (Ge) Phases, the Cubic structure of CsGeBr3 showed an absorption that gradually increased at ~0 eV. Peaks strongly around 12 eV (α ~ 35), then decays above 15 eV. This implies a broad absorption profile, suggesting efficient absorption across a wide range. The tetragonal Ge gave multiple absorption peaks across the range. Strongest absorption near 13 eV (α ~ 38). The Monoclinic Ge generated a sharp rise from ~0.5 eV. Strong absorption plateau between 5–10 eV (α ~ 35–38).

For the Silicon (Si) Phases, the Cubic structure of $CsSiBr_3$ gave an extremely high absorption at < 2 eV (~20,000), then decays rapidly and flattens after ~5 eV. This depicts metallic-like, strong free-carrier absorption rather than interband transitions. The tetragonal Si showed a very weak, fluctuating absorption below ~10 eV. Absorption rises linearly after 10 eV, reaching ~20 at 20 eV. This indicates weak optical activity at low energies for $CsSiBr_3$. Monoclinic Si showed a clear absorption onset at ~0.5 eV. Then a strong, continuous increase up to ~30–35 at ~12–15 eV, where maximum absorption is observed.

The germanium-based perovskite absorbs light in the ultraviolet, visible, and infrared regions, whereas CsSiBr3, on the contrary, has an almost zero absorption coefficient in the visible and infrared regions. The cubic phase exhibits high conductivity applications due to free-carrier behavior. The tetragonal phase exhibits unusual absorption behavior, increasing linearity with the monoclinic phase, which has lower-energy peaks (~1 eV). It is clear from Figure 13 that in the visible and infrared region, the cubic phase of $CsGeBr_3$ shows stronger optical absorption at low energies.

CHAPTER FIVE

SUMMARY, CONCLUSION, AND RECOMMENDATIONS

5.1 Introduction

This chapter provides a detailed summary of the study, which was carried out with the aim of using first-principles computational modeling implemented in the Quantum Espresso software based on DFT. The conclusions and recommendations for the study of the cubic phases CsGeBr3 and CsSiBr3 are presented.

5.2 Summary

The main objective of this study was to determine the structural, optical, elastic, and electronic properties of Ge and Si halide perovskites for solar cell applications. To exploit the promising properties in solar cell applications, it is necessary to identify an appropriate material that improves the stability and the good absorption of Ge- and Si-halide perovskite-based compounds. In this study, calculations of the electronic, structural, elastic, and optical constants of CsGeBr3 and CsSiBr3 were performed, and, since it was based on DFT, computations were restricted to ground-state conditions only.

The results of this study are in agreement with other theoretical predictions and experimental values of 16.5 GPa for $CsGeBr_3$. The Fermi level separates the valence and conduction bands. Among the total DOS, CsGeBr3 and CsSiBr3 showed semiconductor-like properties, as deduced from their band structures. From this work, the absorption of CsGeBr3 and CsSiBr3 began at 2.5eV, with high absorption coefficients, indicating that these materials are suitable for solar cell applications.

Lattice constants obtained for $CsGeBr_3$ and $CsSiBr_3$ are in agreement with experimental and theoretical predictions so far obtained. The Burch-Murnaghan third-order equation of state gave a bulk modulus of 17.97GPa, which corresponds fairly well with the experimental value of 16.5 GPa for $CsGeBr_3$. The $CsGeBr_3$ and $CsSiBr_3$ structure has a wide and direct band gap of 0.7 eV and 0.29 eV, respectively. A shear modulus G of 6.0251 GPa was obtained, indicating that the material is rigid towards reversible deformation. The Young's modulus (E) values of 31.604 GPa and 35.433 GPa for CsGeBr3 and CsSiBr3, respectively, indicate that these materials are tough against linear deformation. Pugh’s ratio (B/G) of 1.793 is lower than 1.95, and the poison’s ratio of 0.26 obtained demonstrates that $CsGeBr_3$ is a ductile material.

5.3 Conclusion

Knowledge of the absorption coefficients, lattice parameters, elastic constants, and band gap of a material helps engineers design and fabricate suitable materials for solar cells. From this study, the results obtained can guide experimentalists in developing CsGeBr3 or CsSiBr3 materials as potential high-performance solar cell absorbers and as benchmarks for developing perovskite solar cells with higher efficiencies.

5.4 Recommendations

This research on the study of the properties of $CsGeBr_3$ and $CsSiBr_3$ recommends the following;

i. The study only dealt with theoretical findings on structural, electronic, dielectric, and elastic properties of $CsGeBr_3$ and $CsSiBr_3$. An experimental study of the cubic, tetragonal, and monoclinic phases of $CsGeBr_3$ and $CsSiBr_3$ is recommended.

ii. The structures were optimized using the Murnaghan equation of state under Quantum Espresso. An extension of this work could be done using another improved exchange-correlation functional.

iii. The band structures, DOS, and charge density maps were only studied in the stable cubic Phase. A study can also be undertaken in the tetragonal and monoclinic phases.

REFERENCES

Alam, Md. (2019). Introductory Chapter: Electrical and Electronic Properties of Materials. 10.5772/intechopen 82360.

Alkauskas, P. Broqvist, A. Pasquarello(2008). *Defect energy levels in density functional calculations: alignment and bandgap problems*, Phys. Rev. Lett. 046405, https://doi.org/10.1103/Phys Rev Lett.101.046405.

Assirey *et al.*(2019). Perovskite synthesis, properties and their related biochemical and Industrial application. Saudi Pharm J.(6):817-829. doi: 10.1016/j.jsps.2019.05.003.

Epub PMID: 31516 324 ; PMCID: PMC6733782.

Bitnar, B. (2003). Silicon, Germanium and Silicon/Germanium Photocells for Thermophotovoltaics Applications. *Semiconductor Science and Technology semicond sci technol. 18*. 10. 1088 /0268-1242/18/5/312.

Born, M. and Huang, K. (1954) Dynamical Theory of Crystal Lattices. Clarendon Press, Oxford.

Burschka, J.*et al;*. (2013). Sequential deposition as a route to high-performance perovskite sensitized solarcells. *Nature*, *499*(7458),316–319. https://doi.org /10. 1038 / nature12340 *Performance Perovskite-Sensitized Solar Cells.* Nature, 499(7458), 316-319.

Cheng, Shangjun & Zhong, Haizheng. (2022). *What Happens When Halide Perovskites Meet*

Cohen, M. L. (1997).Density Functional Theory and Pseudopotentials..International Journal of Quantum Chemistry, 61(4):603–611. *Density Functional Theory in Quantum Chemistry*. 10.1007 /978-4-431-54825-6.

Dai, Xing *et, al.;* (2015). Flexible Light Emitting Diodes Based on Vertical Nitride Nanowire Nano letters. 15. 10.1021/acs.nanolett.5b02900.

Dong, Yifeng & Qin, Lixia & Shi, Liwei & Tang, Gang & Shi, Hongliang.(2013*).* Phase Transition and Band-Structure Tuning in In Through Uniaxial and Biaxial Strains. *Journal of Physics. Condensed Matter*

Fan, J., Jia, B. and Gu, M. (2014) Perovskite-Based Low-Cost and High-Efficiency Hybrid Halide Solar Cells. Photonics Research, 2, 111-120

Feng *et al.*,(2014). Resonant Perovskite Solar Cells with Extended Band www.nature.com

Fischer, C. F (1977).Hartree–Fock Method for Atoms. A numerical Approach. edge. Solar cells. *Photonics Research, (1977).* 2(5), 111-120.

Folk, R. L., & Ward, W. C. (1957). Brazos River bar [Texas]; *A Study in the* Significance of Grain Size Parameters. *Journal of Sedimentary Research, 27*(1), 3-26.

Fredkin and N. R. Werthamer.,(1965). Towards a Quantum Many-Body Theory of LatticeII. Collective Fluctuation Approximation. DOI:https:// doi.org/ 10.1103 /PhysRe

Garnett, *et al* (2008). Silicon Nanowire Radial p−n Junction Solar Cells. J. Am. Chem. Soc. 2008, 130, 9224–9225.

Gao, L., Hu, P., & Liu, S. F. (2023). Low-dimensional Perovskite Modified 3D Structures for Higher-performance Solar Cells. *Journal of Energy Chemistry, 81,* 389-403.

Geisz, J.F., France, R.M., Schulte, K.L. *et al.* (2020). Six-junction III–V Solar Cells with 47.1% Conversion Efficiency under 143 Suns Concentration. Nat Energy **5**, 326–335

Getsoian, *et al*. (2014). Band-Gap Energy as a Descriptor of Catalytic Activity for Propene Oxidation over Mixed Metal Oxide Catalysts. *Journal of the American Chemical Society. 136.* 10.10215.

Giannozzi, P.et al;.. (2009). Quantum Espresso*: A* Modular and Open-source Software Project for Quantum Simulations of Materials.

Grånäs, O., Vinichenko, D., & Kaxiras, E. (2016). Establishing the Limits of Efficiency of Perovskite Solar Cells from First Principles Modeling. Scientific Reports, 6, 36108

He *et al*.,(2002).Industrial Viability of Single Component Organic Solar Cells. https:// www.sciencedirect.com

Hill A.V,(1932). The Thermodynamic Elasticity in perovskites. https://www .jstor.org>stable

Hohenberg, P. and Kohn, W. (1964).*Inhomogeneous Electron Gas*. Physical Review B, 136, 864- 871. http://dx.doi.org/101103/Phys Rev. 136.B864

Hou T.S.,*et al* (2008). Formation Mechanism and Stability Analysis.https ://www.researc hgate.net

Houari, Mohammed et al;., (2019). *Optoelectronic Properties of Germanium Iodide Perovskites AGeI3 (A = K, Rb and Cs): First Principles Investigations*. Optical and Quantum Electronics. 51. 10.1007/s11082- 019-1949

Jian *et al*,(2011*). Inorganic– organic Halide Perovskites for New Photovoltaic Technology, National S cience Review,* Volume 5, Pages 559– 576,

Jayadeep D.R (2007).Mechanical Properties of Silicon Carbide (SiC) Thin Films. University of South Florida. Graduate Theses and Dissertations. *Organic/Inorganic Perovskites for Photovoltaic Applications,*" J. Phys. Chem. Lett., vol.4 no. 17, pp. 2999–3005, 2013, doi: 10.1021 /jz401

Jong *et al*.,(2019). First-Principles Study on Structural, Electronic, and Optical Properties of In organic Ge-Based Halide Perovskites. *Inorganic Chemistry. 58.* 10.1021 /acs .inorg che . 8b03095.

Jong *et al.*,(2020). Stable Perovskites Solar Cells with Efficiency Exceeding 24.8% and *0.3V* Voltage Loss.DOI:10.1126/science.abb7167

J. Qian, B. Xu, and W. Tian, (2016) "A Comprehensive Theoretical Study of Halide Perovskites ABX3," *Org. Electron., vol. 37,* pp. 61–73.

Kanatzidis *et al.,*(2006). Effect of Thermo-mechanical Treatment on Mechanical Properties and Memory Behavior of Tiâ€“(26â€“28)at.% Nb alloys. *Materials Science and Engineering:* A. 438. 839-843

Kanatzidis *et al.,*(2015). Superior Thermoelectric Performance in PbTe PbS.Sci.,2015 2056 DOI: 10:1039/ c5EE01147G

Kohn, W.and Hohenberg, P. and (1964). Inhomogeneous Electron Gas. *Physical Review B, 136,* 864-871.

Kohn and L. J. Sham (1965*). Self-Consistent Equations Including Exchange and Correlation Effects*. DOI:https://doi.org/10.1103/PhysRev.140.A1133

Kokalj A.,(1999). *Journal of Molecular Graphics and Modelling*. https//doi.org /10.1016/S1093- 3263(99)00028-5

Kleinman L. and D. M. Bylande r(1982). "*Efficacious Form for Model Pseudopotentials," Letters,* Vol. 48, No. 20, 1982, pp. 1425-1428.

Krishnamurthy, C., Balasubramaniam, K., & Ravindran, P. (2015). Wave Propagation Through Isotropic, Linear Elastic Material Using Mass Spring Lattice Model. National Seminar & Exhibition on Non-Destructive Evaluation, NDE 2011,

Lin, L. *et al* (2017).Modeling and Analysis of HTM-free Perovskite Solar Cells Based on Zn Electron Transport Layer, Superlattice.167–177.

Ling M. (2017).Correlation of Optical Properties, Electronic Structure, and Photocatalytic Activity in Nanostructured Tungsten Oxide.

Liu T. (2006). DFT Description on Electronic Structure and Optical Absorption Properties of Anionic S-doped Anatase TiO2, J. Phys. Chem. B 110 17866–17871.

Liu, M., Johnston, M. & Snaith, H. (2013). *Efficient Planar Heterojunction Perovskite Solar Cells by Vapour Deposition n. Nature* **501**, 395–398

Logothetidis, S. (2012). *Nanostructured Materials and Their Applications.*10.1007/978-3642-22227

Madeeha A. *et al* (2020).*Organic Inorganic Perovskites: A Low-Cost-Efficient Photovoltaic Material. Published: January 27th 2021.*

Madsen *et al.*(2016).*First Principle Calculations to Investigate Structural,Electronic and Optical Properties of Heavy Perovskites*. https://doi.org/10.1016/j.mseb.2022. 115781.

MD Arif *et al.* (2024). *Effect of Low to High Pressure on the Structural, Mechanical, Electrical,and Optical Properties of Inorganic Material Ca_3AsBr_3*: An Ab Initio Investigation.ACS Omega,2024.

Martin *et al.,*(2020). *Solar Cell efficiency Tables (Conversion 55).* National Renewable Energy laboratory.https://researchhub.nrel.gov

Ming *et al.,*(2023).*Thin film absorber for Tandem Solar cells*: An Industrial perspective. Vol.5 *Journal for Physics* DOI:10.1088/2515- 7655/acff18

Mitzi, D. B., Wang, S., Feild, C. A., Chess, C. A., & Guloy, A. M. (1995). *Conducting Layered anic-inorganic Halides Containing <110>-Oriented Perovskite*. Sheets *Science (New York, N.Y.), 267*(5203), 1473–1476.

Miyasaka *et al.*,(2006). Organometal Halide Perovskite as Visible-Light Sensitizers for photovoltai cell. *Journal for American Chemical Society*. DOI:10.1021/ja809598r

Mohamed M.,(2020). *Equation of State.*https://www.intechopen.com

Monkhorst, H.J. and Pack, J.D. (1976) Special Points for Brillouin-Zone Integrations.*Physical Review B, 13,* 5188-5192. http://dx.doi.org /10.1103/ PhysRevB.13.5188

Mouhat, F. and Coudert, F.X. (2014). Necessary and Sufficient Elastic Stability Conditions in Various Crystal Systems. Physical Review B, 90, Article ID: 224104.

Mudasser R N. & Noureddine, S. & Al-Shaalan, N. & Alharthi, S. & Alharthy, S, & Amin, M. & Tirth, V. & Khan, R. & Sohail, M & Azzouz R., A. & Khattak, S. & Khan, M. (2023). *The omparative Investigations of Structural, Optoelectronic, and Mechanical Properties of AgBeX3 (X = F and Cl) Metal Halide-Perovskites for Prospective Energy Applications Utilizing DFT Approach*. Optical and Quantum Electronics. 55. 10.1007/s11082-023-05187-9.

Muhammad A. Alam and M, Ryan (2019). *Shockley- Queisser Triangle Predicts the Thermodynamic Efficiency Limits of Arbitrarilyt Complex Multijunction Bifacial Solar Cells*. https://doi.org/10.1073/pnas.1910745116.

Nam-Gyu P.,(2015).*Perovskite Solar Cells: an Emerging Photovoltaic Technology, Materials Today,*.Volume 18, Issue 2, 2015, Pages 65-72,

Noel N. *et al* (2014).*Lead-free Organic–inorganic Tin Halide Perovskites for Photovoltaic Applications* Crossref DOI link:https://doi.o rg/10.1039/ C4EE0 10\76K

Orio *et al.*,(2009). High efficiency Crystalline Silicon Solar Cells: Status and Perspective. https://pubs.rsc.org

Park *et al.*,(2015). In Research and Application ; https://doi.org/10.1039/C4EE01076K

Perdew *et al.*,(2016).*Enhancing Solar Cell Efficiency Beyond 27% through the Implementation of Efficient Charge Carrier*. Volume 190.http://doi.org/10.1016 /j.jpcs 2016.

Perdew, J. & Zunger, Alex. (1981). Self-Interaction Correction to Density- Functional for Many- Systems. Phys. Rev. B. 23. 5048-5079. 10.1103/PhysRevB.23.5048.

Pugh,S.(1954).*Relations between Elastic Moduli and Plastic Properties of Pure Metals.*The London, Edinburg and Dublin philosophical magazine and journal of science,45(376),823-843

Rai D.,(2017).*Analysis of Various ETL Materialsfor an Efficient Perovskite Solar Cell by Numerical Simulation*. Volume 31, pages 16269-16280.,(2017).

R. Ali *et al*., (2010).“*Compositional Engineering Study of Lead-Free Hybrid Perovskites for* 10.1021/acsami.0c14595.

Raghvendra,.*et al* (2019).*Performance Evaluation and Material Parameter Perspective of Eco- friendly Highly Efficient CsSnGeI3 Perovskite Solar Cell,* Superlattices Microstruct. 135 (2019), 106273.

Ran,*et al.,* (2009). *One-dimensional Topologically Protected Modes in Topological Insulators with Lattice Dislocations. Nature Physics*, 5(4):298.

Rubio L. (2020). Handbook of Materials Modeling: Methods: Theory and Modeling 10.1007. /978- 3-319-42913-7.

Salem, M.S.*et al*.(2008). *Design and Simulation of Proposed Low Cost Solar Cell Structures Based on Heavily Adoped Silicon Wafers. In Proceedings of the 2016 IEEE 43rd Photovoltaic Specialists Conference (PVSC*), Portland, OR, USA, 5–10 June 2016; pp. 2393–2397

Saparov, B., & Mitzi, D. B. (2016). *Organic–inorganic Perovskites: Structural Versatility for Functional Materials Design*. Chemical reviews, 116(7), 4558-

ssss 596.

Singh P.K. & Dwivedi (2012). *Review on Perovskite Solar Cells via Vacuum and Non-vacuum Methods*. https://doi.org/10.1016/j.rsurfi.2012.100210

Singh, P.K. & Dwivedi, A.. (2012). Pressure Derivatives of Bulk Modulus Materials at Extreme Compression. *Indian Journal of Pure and Applied Physics. 50.*734-738.

Sholl, D. & Steckel, J.(2011).*Density Functional Theory: a Practical Introduction* {https:// api.semanticscholar. org/CorpusID:93264228}

Slater *et al* (1930). Better Performance of Hartree–Fock over DFT: a Quantum Mechanical Investigation on Pyridinium Benzimidazolate Typesof Zwitterions in the Ligh of Localization/ Delocalization issues. *Journal of Molecular Modeling. 29.*

Soler *et al* (2002) *J.Phys.: Condens. Matter* 14 2745. DOI 10.1088 /09538984/14/11/302

Stranks, S. D., Eperon, G. E., Grancini, G., Menelaou, C., Alcocer, M. J., Leijtens, T.,& Snaith H. J. (2013). *Electron-hole Diffusion Lengths Exceeding Micrometer in an Organometal Trihalide Perovskite.*

TaS. Zhu, J. Ye, Y. Zhao, and Y. *Qiu.(2019).“Structural, Electronic, Stability, and Optical Properties* of *CsPb1- xSn xIBr2 Perovskites*: vol. 123, no. 33, pp. 20476–20487, 2019,

T., Che, F., Wei, M., Zhao, Y., Saidaminov, M. I., Sargent, E.H. (2018). *Dipolar Cations Confer Defect Tolerance in Wide-bandgap Metal Halide Perovskites. Nature Communication 9(1)*

Tang, M.; Li, Z.; Wang, K.; Jiang, Y.; Tian, M.; Qin, Y.; Gong, Y.; Li, Z.; Wu, L (2022). *Ultrafast Self- Healing and Self-Adhesive Polysiloxane towards Reconfigurable on-Skin Electronics.* J. Mater. Chem, 10.

Trofimov, P.; Pushkarev, A.P.; Sinev, I.S.; Fedorov, V.V.; Bruyère, S.;Bolshakov, A.; Makarov,S.V. (2020). *Perovskite–Gallium Phosphide Platform for Reconfigurable* Visible- Lianophotonic

Troullier, N. and Martins, J. (1990). *A Straightforward Method for Generating Soft Transferable Pseudopotentials*. Solid State Communications, 74(7):613–616.

Tsang, D. P., Matsushima, T., & Adachi, C. (2016). *Operational Stability Enhancement in Organic Light-emitting Diodes with Ultrathin Liq Interlayers*. *Scientific Reports, 6*, 22463.

Tyuterev,V.G and Vast, N.(2006).*Murnaghan's Equation of State for the Elecrtronic Ground State Energy*.https://doi.org/10.1016/j.commatsci.2005.08.012

Tyuterev,V.G and Tremedous,G (2006).*Ab Initio Effective Rotational Hamiltonians*. A comparative Study, hal-00588499v1

UNIST (2021). *Perovskite Solar Cell Efficiency*. https://taiyangnews.info

Varmo P. C. (2018). *Low-dimensional Perovskites.* Science direct 1

Wang, Wei & Shao, Zongping. (2024). *Lead-Free All-Inorganic Cesium Bismuth Iodide Perovskite Solar Cells:* Recent Advances, Current Limitations, and Future Prospects. Solar RRL. 8. 10.1002/solr.202300984.

Wang, T.; Wang, R.; Cheng, Y.; Sun, J,.(2016). *Quasi In Situ Polymerization To Fabricate Copper Nanowire-Based Stretchable Conductor and Its Applications*. ACS Appl. Mater. Interfaces 8,9297–9304

Woods N. D., Payne M. C. and Hasnip P. J., (2019).Computing the Consistent Field in Kohn-Sham Density Functional Theory.*Journal of physics: condensedmatter 31*:45

W. Isoe, M. Mageto, M. Maghanga, M. Mwamburi, V. Odari, C. Awino.(2020). *Thickness ependence of Window Layer on CH3NH3PbI3-XClX Perovskite Solar Cell Hindawi Int.* Photoenergy pp. 1-7, 10.1155/2020/8877744.

Xiang-Bin & Zhang, Wen. (2017). *Structural Phase Transitions and Dielectric Switching in a Series of Organic-Inorganic Hybrid Perovskites ABX3 (X=ClO4 - or BF4 -).* Chemistry (Weinheim an der Bergstrasse, Germany). 23. 10.1002/chem.201702228

Xing G. C , N. Mathews, S.Y. Sun, S.S. Lim, Y.M. Lam, M. Graetzel, S. Mhaisalkar, T.C. Sum. (2013). *Long-range Balanced Electron- and Hole-transport Lengths in Organic-inorganic CH 3 NH3 PbI 3* Science 342, 344–347

Yu-Ling S.et al (2017).*Structural Phase Transitions and Dielectric Switching in a Series of Organic- Inorganic Hybrid Perovskites ABX3.*

Young Kim, Doh-Kwon Lee, Dae-Eun Kim, Jinwoo Lee, Min Jae Ko(2015). *Highly Efficient Perovskite Solar Cells Based on Mechanically Durable Molybdenumcathode, Nano Energy*.Volume 17, Pages 131-139,

Yang, T.-C.; Lee, B.-S.; Yen, T.-J. (2012).*Minimizing Reflection Losses from Metallic Electrodes and Enhancing Photovoltaic Performance using the Si-micrograting Solar celL with Vertical Sidewall lectrodes*.Appl. Phys. Lett. 101,103902.

Zekry A., Yahyaoui I., Tadeo F., (2019). *Generic Analytical Models for Organic and Perovskite Solar Cells,* The 10th International Renewable Energy Congress (IREC)

Zhang, X. F., Liu, Z. G., Shen, W., & Gurunathan, S. (2016). Silver Nanoparticles: Synthesis, Characterization, Properties, Applications and Therapeutic Approaches. *International Journal of molecular sciences, 17* (9),1534.

Zhang, J. M.*et al*. (2018). A DFT *Study on Structural Evolution, Electronic Property and Spectral Analysis of Yttrium- doped Germanium Clusters*. Molecular Physics, 121 (5)

Zhou, C., Lin, H., Lee, S., Chaaban, M., &MA. B., (2018). *Organic-inorganic Halide Hybrids Beyond Perovskites*. Material Research Letters, 6.

APPENDICES

Appendix I: Input File for Pwscf Code CsGeBr$_3$ structure

This software is an integral component of the open-source Quantum ESPRESSO suite, which facilitates quantum simulations of materials. For any publications or presentations that result from the use of this program, please reference the following works: "P. Giannozzi et al., J. Phys.: Condens. Matter 21 395502 (2009);" and "P. Giannozzi et al., J. Phys.: Condens. Matter 29 465901 (2017);" along with the URL http://www.quantum-espresso.org. Additional information can be found at http://www.quantum-espresso.org/quote. The parallel version of this program, utilizing MPI, is currently operating on 48 processors, with the MPI processes distributed across 2 nodes. The division of R & G space is configured as proc/nbgrp/npool/nimage = 48. The program is now awaiting input and is reading from the standard input. The current specifications for the PWSCF program are as follows: the maximum number of distinct atomic species (ntypx) is 10, the maximum number of k-points (npk) is 40,000, and the maximum angular momentum in pseudopotentials (lmaxx) is 3. Atomic positions and the unit cell have been retrieved from the directory: ./out/aiida.save/. In the iterative solution of the eigenvalue problem, subspace diagonalization will employ one subgroup per band group, utilizing a ScaLAPACK distributed-memory algorithm with a subgroup size of 4 * 4 processors.

```
& CONTROL
    calculation = 'scf'
    restart_mode='from_scratch',
    outdir = './'
    prefix = 'aiida'
    pseudo_dir = '/mnt/lustre/users/mnamisi/ken/pseudos'
    tprnfor = .true.
    tstress = .true.
    verbosity = 'high'
   &SYSTEM
    degauss =   1.4699723600d-02
    ecutrho =   400
    ecutwfc =   50
```

```
  celldm(1) = 10.5971
  ibrav = 1
  nat = 5
  nosym = .false.
  ntyp = 3
  occupations = 'smearing'
  smearing = 'm-v'
&ELECTRONS
  conv_thr =   1.0000000000d-09
  electron_maxstep = 80
  mixing_beta =   0.7
ATOMIC_SPECIES
Br     79.904 br_pbe_v1.4.uspp.F.UPF
Cs     132.9054519 Cs_pbe_v1.uspp.F.UPF
Ge     72.64 ge_pbe_v1.4.uspp.F.UPF
ATOMIC_POSITIONS crystal
Cs          0.0000000000       0.0000000000       0.0000000000
Ge          0.5000000000       0.5000000000       0.5000000000
Br          0.5000000000       0.5000000000      -0.0000000000
Br          0.5000000000       0.0000000000       0.5000000000
Br          0.0000000000       0.5000000000       0.5000000000
K_POINTS automatic
8 8 8 0 0 0
```

Appendix II: Input File for Pwscf Code CsSiBr3 structure

```
 &CONTROL
    calculation = 'scf'
    restart_mode='from_scratch',
    outdir = './'
    prefix = 'aiida'
    pseudo_dir = '/mnt/lustre/users/mnamisi/ken/pseudos'
    tprnfor = .true.
    tstress = .true.
    verbosity = 'high'
   &SYSTEM
    degauss =   1.4699723600d-02
    ecutrho =   400
    ecutwfc =   50
    celldm(1) = 10.3593
    ibrav = 1
    nat = 5
    nosym = .false.
    ntyp = 3
    occupations = 'smearing'
    smearing = 'm-v'
   &ELECTRONS
    conv_thr =   1.0000000000d-09
    electron_maxstep = 80
    mixing_beta =   0.7
```

```
ATOMIC_SPECIES
Br     79.904 br_pbe_v1.4.uspp.F.UPF
Cs     132.9054519 Cs_pbe_v1.uspp.F.UPF
Si     28.0855 Si.pbe-n-rrkjus_psl.0.1.UPF
ATOMIC_POSITIONS crystal
Cs           0.0000000000       0.0000000000       0.0000000000
Si           0.5000000000       0.5000000000       0.5000000000
Br           0.5000000000       0.5000000000      -0.0000000000
Br           0.5000000000       0.0000000000       0.5000000000
Br           0.0000000000       0.5000000000       0.5000000000
K_POINTS automatic
8 8 8 0 0 0
```

Appendix III: Input File for CsGeBr3 Elastic Constants

```
        calculation = 'scf'
    restart_mode='from_scratch',
    outdir = './'
    prefix = 'aiida'
    pseudo_dir = '/mnt/lustre/users/mnamisi/ken/pseudos'
    tprnfor = .true.
    tstress = .true.
    verbosity = 'high'
   &SYSTEM
    degauss =   1.4699723600d-02
    ecutrho =   400
    ecutwfc =   50
    celldm(1) = 10.5971
    ibrav = 1
    nat = 5
    nosym = .false.
    ntyp = 3
    occupations = 'smearing'
    smearing = 'm-v'
   &ELECTRONS
    conv_thr =   1.0000000000d-09
    electron_maxstep = 80
    mixing_beta =   0.7
   ATOMIC_SPECIES
   Br     79.904 br_pbe_v1.4.uspp.F.UPF
   Cs     132.9054519 Cs_pbe_v1.uspp.F.UPF
   Ge     72.64 ge_pbe_v1.4.uspp.F.UPF
MPI processes distributed on     2 nodes
     R & G space division:  proc/nbgrp/npool/nimage =48
      Reading input from _temporary_1
    Info: using nr1, nr2, nr3 values from input
    Computing the elastic constants at the minimum volume
```

```
FFT mesh: (   72,   72,   72 )
   Bravais lattice:
   ibrav=  1: simple cubic
   Cell parameters:
   alat=  10.597100 a.u.
Starting primitive lattice vectors:
   crystal axes: (cart. coord. in units of alat)
          a(1) = (   1.000000   0.000000   0.000000 )
           a(2) = (   0.000000   1.000000   0.000000 )
           a(3) = (   0.000000   0.000000   1.000000 )
  Starting reciprocal lattice vectors:
   reciprocal axes: (cart. coord. in units 2 pi/alat)
          b(1) = (  1.000000  0.000000  0.000000 )
           b(2) = (  0.000000  1.000000  0.000000 )
           b(3) = (  0.000000  0.000000  1.000000 )
   Starting atomic positions in Cartesian axes:
   site n.     atom                  positions (alat units)
      1           Cs  tau(   1) = (   0.0000000   0.0000000   0.0000000  )
      2           Ge  tau(   2) = (   0.5000000   0.5000000   0.5000000  )
      3           Br  tau(   3) = (   0.5000000   0.5000000   0.0000000  )
      4           Br  tau(   4) = (   0.5000000   0.0000000   0.5000000  )
      5           Br  tau(   5) = (   0.0000000   0.5000000   0.5000000  )
   Starting atomic positions in crystallographic axes:
   site n.     atom                  positions (cryst. coord.)
      1           Cs  tau(   1) = (  0.0000000  0.0000000  0.0000000  )
      2           Ge  tau(   2) = (  0.5000000  0.5000000  0.5000000  )
      3           Br  tau(   3) = (  0.5000000  0.5000000  0.0000000  )
      4           Br  tau(   4) = (  0.5000000  0.0000000  0.5000000  )
      5           Br  tau(   5) = (  0.0000000  0.5000000  0.5000000  )
   Total mass of this unit cell        445.2575 a.m.u.
   Density of this solid              4192.72 kg/m^3        4.1927 g/cm^3
Parallelization info
   sticks:   dense  smooth     PW     G-vecs:    dense   smooth      PW
   Min          71      35     10               3157     1117     172
   Max          72      36     12               3162     1122     175
```

```
     Sum        3433    1725    497              151635    53715    8289
     bravais-lattice index     =            1
     lattice parameter (alat)  =      10.3971  a.u.
     unit-cell volume          =    1123.9233 (a.u.)^3
     number of atoms/cell      =            5
     number of atomic types    =            3
     number of electrons       =        44.00
     number of Kohn-Sham states=           26
     kinetic-energy cutoff     =      50.0000  Ry
     charge density cutoff     =     400.0000  Ry
     convergence threshold     =      1.0E-09
     mixing beta               =       0.7000
     number of iterations used =            8  plain     mixing
     Exchange-correlation=  SLA  PW   PBX  PBC
                           (   1   4   3   4   0   0   0)
     nstep                     =           20
    BFGS Geometry Optimization
     bfgs converged in   1 scf cycles and   0 bfgs steps
     (criteria: energy <  1.0E-04 Ry, force <  1.0E-03 Ry/Bohr)
     End of BFGS Geometry Optimization
     Final energy   =    -417.6696402923 Ry
      Begin final coordinates
   ATOMIC_POSITIONS (crystal)
  Cs            0.0000000000        0.0000000000        0.0000000000
  Ge            0.5000000000        0.5000000000        0.5000000000
  Br            0.5000000000        0.5000000000       -0.0000000000
  Br            0.5000000000       -0.0000000000        0.5000000000
  Br           -0.0000000000        0.5000000000        0.5000000000
  End final coordinates
Writing output data file .//g8/aiida.save/
   Elastic constant     3    3
  strain        stress (kbar)
     -0.0075000000      3.4908733529
     -0.0025000000      1.0377934863
```

```
  0.0025000000    -1.3157953938
  0.0075000000    -3.5356393332
 Polynomial coefficients
 a1= -0.104400355399E-05
 a2= -0.318590371959E-02
 a3=  0.158550587423E-01
 Elastic constant     1    3
  strain       stress (kbar)
 -0.0075000000      0.6034545953
 -0.0025000000      0.1040516830
  0.0025000000    -0.4161640423
  0.0075000000    -0.9204083316
Polynomial coefficients
 a1= -0.105879158704E-05
 a2= -0.692267786475E-03
 a3= -0.329110169811E-03
Elastic constant     4    4
 strain       stress (kbar)
 -0.0075000000      1.4363315890
 -0.0025000000      0.4798697648
  0.0025000000    -0.4815352294
  0.0075000000    -1.4511564565
 Polynomial coefficients
 a1= -0.698112450532E-10
 a2= -0.130843487262E-02
 a3= -0.894558178058E-03
 Elastic constants C_ij (kbar)
i j=       1           2           3           4           5           6
1   468.66254   101.83609   101.83609     0.00000     0.00000     0.00000
2   101.83609   468.66254   101.83609     0.00000     0.00000     0.00000
3   101.83609   101.83609   468.66254     0.00000     0.00000     0.00000
4     0.00000     0.00000     0.00000    96.23869     0.00000     0.00000
5     0.00000     0.00000     0.00000     0.00000    96.23869     0.00000
6     0.00000     0.00000     0.00000     0.00000     0.00000    96.23869
```

```
    1 bar = 10^5 Pa; 10 kbar = 1 GPa; 1 atm = 1.01325 bar; 1 Pa = 1 N/m^2
    1 Pa = 10 dyn/cm^2; 1 Mbar = 10^11 Pa
    1 torr = 1 mm Hg = 1/760 bar = 7.5006 x 10^-3 Pa
  Elastic compliances  S_ij (1/Mbar)
   i j=      1          2          3          4          5          6
   1     2.31317   -0.41291   -0.41291    0.00000    0.00000   -0.00000
   2    -0.41291    2.31317   -0.41291    0.00000    0.00000   -0.00000
   3    -0.41291   -0.41291    2.31317    0.00000    0.00000   -0.00000
   4     0.00000    0.00000    0.00000   10.39083    0.00000   -0.00000
   5     0.00000    0.00000    0.00000    0.00000   10.39083   -0.00000
   6     0.00000    0.00000    0.00000    0.00000    0.00000   10.39083
    1/Mbar = 1/10^{11} Pa; 1 Pa = 1 N/m^2
    Voigt approximation:
    Bulk modulus  B =    224.11157 kbar
    Young modulus E =    329.14136 kbar
    Shear modulus G =    131.10850 kbar
    Poisson Ratio n =      0.25523
    Reuss approximation:
    Bulk modulus  B =    224.11157 kbar
    Young modulus E =    302.94704 kbar
    Shear modulus G =    118.83024 kbar
    Poisson Ratio n =      0.27471
    Voigt-Reuss-Hill average of the two approximations:
    Bulk modulus  B =    224.11157 kbar
    Young modulus E =    316.04420 kbar
    Shear modulus G =    124.96937 kbar
    Poisson Ratio n =      0.26449
    Voigt-Reuss-Hill average; sound velocities:
    Compressional V_P =     3051.797 m/s
    Bulk          V_B =     2311.241 m/s
    Shear         V_G =     1725.897 m/s

 This run was terminated on:  21: 4:36  24Jan2023
 =   JOB DONE.
```

Appendix IV: Output File for CsSiBr3 Elastic Constants

```
 &CONTROL
  calculation = 'scf'
  restart_mode='from_scratch',
  outdir = './'
  prefix = 'aiida'
  pseudo_dir = '/mnt/lustre/users/mnamisi/ken/pseudos'
  tprnfor = .true.
  tstress = .true.
  verbosity = 'high'
&SYSTEM
  degauss =   1.4699723600d-02
  ecutrho =   400
  ecutwfc =   50
  celldm(1) = 10.3593
  ibrav = 1
  nat = 5
  nosym = .false.
  ntyp = 3
  occupations = 'smearing'
  smearing = 'm-v'
&ELECTRONS
  conv_thr =   1.0000000000d-09
  electron_maxstep = 80
  mixing_beta =   0.7
ATOMIC_SPECIES
Br     79.904 br_pbe_v1.4.uspp.F.UPF
Cs     132.9054519 Cs_pbe_v1.uspp.F.UPF
Si     28.0855 Si.pbe-n-rrkjus_psl.0.1.UPF
ATOMIC_POSITIONS crystal
Cs           0.0000000000       0.0000000000       0.0000000000
Si          0.5000000000       0.5000000000       0.5000000000
Br           0.5000000000       0.5000000000      -0.0000000000
Br           0.5000000000       0.0000000000       0.5000000000
Br           0.0000000000       0.5000000000       0.5000000000
K_POINTS automatic
8 8 8 0 0 0
```

Appendix V: Output File for CsGeBr3 Elastic Constants

This software is an integral component of the open-source Quantum ESPRESSO suite, which facilitates quantum simulations of materials. For any publications or presentations that result from the use of this program, please reference the following works: "P. Giannozzi et al., J. Phys.: Condens. Matter 21 395502 (2009);" and "P. Giannozzi et al., J. Phys.: Condens. Matter 29 465901 (2017);" along with the URL http://www.quantum-espresso.org. Additional information can be found at http://www.quantum-espresso.org/quote. The parallel version of this program, utilizing MPI, is currently operating on 48 processors, with the MPI processes distributed across 2 nodes. The division of R & G space is configured as proc/nbgrp/npool/nimage = 48. The program is now awaiting input and is reading from the standard input. The current specifications for the PWSCF program are as follows: the maximum number of distinct atomic species (ntypx) is 10, the maximum number of k-points (npk) is 40,000, and the maximum angular momentum in pseudopotentials (lmaxx) is 3. Atomic positions and the unit cell have been retrieved from the directory: ./out/aiida.save/. In the iterative solution of the eigenvalue problem, subspace diagonalization will employ one subgroup per band group, utilizing a ScaLAPACK distributed-memory algorithm with a subgroup size of 4 * 4 processors.

> The information regarding parallelization has been generated using the Vanderbilt code, version 7.3.6, authored by kfg, with the generation date recorded as May 13, 2013. The original format has been automatically converted, and the Pseudo was produced through a Scalar-Relativistic Calculation. The local potential cutoff radius is specified as 2.30000000000E+00, with various parameters such as nl, pn, l, occupancy, Rcut, Gcut, and pseudopotential values detailed for different orbital types, including 5S, 5P, 5D, 6S, and 6P.

The header section provides essential details, including the version number, the element being analyzed (Cs), and the type of pseudopotential employed (Ultrasoft). It also indicates the presence of a Nonlinear Core Correction and specifies the exchange-correlation functional used, which is the PBE. The valence Z is noted as 9.00000000000, with the total energy calculated at -63.00384417630. Suggested cutoffs for wavefunctions and charge density are both indicated as 0.00000, while the maximum angular momentum component is set at 2, and the mesh comprises 905 points. The number of wavefunctions and projectors is recorded as 5 and 6, respectively, with detailed occupancy values for the various wavefunctions.

The mesh section outlines the radial coordinates, beginning from 0.00000000000E+00 and extending to 5.67720230969E-06, providing a comprehensive range of values. Additionally, the PP_DIJ subsection lists the number of nonzero Dij values, which totals nine. Each entry specifies the indices and corresponding Dij values, illustrating the interactions between different components, with notable values such as 1.29207215929E+00, -1.76637262031E+00, and 1.39232024315E+00, among others, reflecting the complexity of the system being analyzed.

```
  MPI processes distributed on     2 nodes
  R & G space division:  proc/nbgrp/npool/nimage =48
   Reading input from _temporary_1
 Info: using nr1, nr2, nr3 values from input
Computing the elastic constants at the minimum volume
 FFT mesh: (   72,   72,   72 )
   Bravais lattice:
   ibrav=  1: simple cubic
   Cell parameters:
   alat=  10.597100 a.u.
 Starting primitive lattice vectors:
   crystal axes: (cart. coord. in units of alat)
          a(1) = (   1.000000   0.000000   0.000000 )
           a(2) = (   0.000000   1.000000   0.000000 )
           a(3) = (   0.000000   0.000000   1.000000 )
  Starting reciprocal lattice vectors:
   reciprocal axes: (cart. coord. in units 2 pi/alat)
          b(1) = (  1.000000  0.000000  0.000000 )
           b(2) = (  0.000000  1.000000  0.000000 )
           b(3) = (  0.000000  0.000000  1.000000 )
   Starting atomic positions in Cartesian axes:
   site n.     atom                 positions (alat units)
```

```
     1           Cs  tau(   1) = (   0.0000000   0.0000000   0.0000000  )
     2           Ge  tau(   2) = (   0.5000000   0.5000000   0.5000000  )
     3           Br  tau(   3) = (   0.5000000   0.5000000   0.0000000  )
     4           Br  tau(   4) = (   0.5000000   0.0000000   0.5000000  )
     5           Br  tau(   5) = (   0.0000000   0.5000000   0.5000000  )
   Starting atomic positions in crystallographic axes:
   site n.     atom                  positions (cryst. coord.)
     1           Cs  tau(   1) = (  0.0000000  0.0000000  0.0000000  )
     2           Ge  tau(   2) = (  0.5000000  0.5000000  0.5000000  )
     3           Br  tau(   3) = (  0.5000000  0.5000000  0.0000000  )
     4           Br  tau(   4) = (  0.5000000  0.0000000  0.5000000  )
     5           Br  tau(   5) = (  0.0000000  0.5000000  0.5000000  )
Parallelization info
   sticks:   dense  smooth     PW     G-vecs:    dense   smooth      PW
   Min          71      35     10               3157     1117     172
   Max          72      36     12               3162     1122     175
   Sum        3433    1725    497             151635    53715    8289
   bravais-lattice index     =            1
   lattice parameter (alat)  =      10.3971  a.u.
   unit-cell volume          =    1123.9233 (a.u.)^3
   number of atoms/cell      =            5
   number of atomic types    =            3
   number of electrons       =        44.00
   number of Kohn-Sham states=           26
   kinetic-energy cutoff     =      50.0000  Ry
   charge density cutoff     =     400.0000  Ry
   convergence threshold     =      1.0E-09
   mixing beta               =       0.7000
   number of iterations used =            8  plain     mixing
   Exchange-correlation=  SLA  PW   PBX  PBC
                         (   1   4   3   4   0   0   0)
   nstep                     =           20
  ATOMIC_POSITIONS (crystal)
Cs           0.0000000000        0.0000000000        0.0000000000
```

```
  Ge           0.5000000000       0.5000000000       0.5000000000
  Br           0.5000000000       0.5000000000      -0.0000000000
  Br           0.5000000000      -0.0000000000       0.5000000000
  Br          -0.0000000000       0.5000000000       0.5000000000
  End final coordinates
Writing output data file .//g8/aiida.save/
     Elastic constant     3    3
    strain       stress (kbar)
       -0.0075000000      3.4908733529
       -0.0025000000      1.0377934863
        0.0025000000     -1.3157953938
        0.0075000000     -3.5356393332
       Polynomial coefficients
       a1= -0.104400355399E-05
       a2= -0.318590371959E-02
       a3=  0.158550587423E-01
       Elastic constant     1    3
        strain       stress (kbar)
       -0.0075000000      0.6034545953
       -0.0025000000      0.1040516830
        0.0025000000     -0.4161640423
        0.0075000000     -0.9204083316
      Polynomial coefficients
       a1= -0.105879158704E-05
       a2= -0.692267786475E-03
       a3= -0.329110169811E-03
      Elastic constant     4    4
       strain       stress (kbar)
       -0.0075000000      1.4363315890
       -0.0025000000      0.4798697648
        0.0025000000     -0.4815352294
        0.0075000000     -1.4511564565
       Polynomial coefficients
       a1= -0.698112450532E-10
```

```
 a2= -0.130843487262E-02
 a3= -0.894558178058E-03
 Elastic constants C_ij (kbar)
i j=      1          2          3          4          5          6
1   468.66254   101.83609   101.83609     0.00000     0.00000     0.00000
2   101.83609   468.66254   101.83609     0.00000     0.00000     0.00000
3   101.83609   101.83609   468.66254     0.00000     0.00000     0.00000
4     0.00000     0.00000     0.00000    96.23869     0.00000     0.00000
5     0.00000     0.00000     0.00000     0.00000    96.23869     0.00000
6     0.00000     0.00000     0.00000     0.00000     0.00000    96.23869
 1 bar = 10^5 Pa; 10 kbar = 1 GPa; 1 atm = 1.01325 bar; 1 Pa = 1 N/m^2
 1 Pa = 10 dyn/cm^2; 1 Mbar = 10^11 Pa
 1 torr = 1 mm Hg = 1/760 bar = 7.5006 x 10^-3 Pa
Elastic compliances  S_ij (1/Mbar)
i j=      1          2          3          4          5          6
1     2.31317    -0.41291    -0.41291     0.00000     0.00000    -0.00000
2    -0.41291     2.31317    -0.41291     0.00000     0.00000    -0.00000
3    -0.41291    -0.41291     2.31317     0.00000     0.00000    -0.00000
4     0.00000     0.00000     0.00000    10.39083     0.00000    -0.00000
5     0.00000     0.00000     0.00000     0.00000    10.39083    -0.00000
6     0.00000     0.00000     0.00000     0.00000     0.00000    10.39083
 1/Mbar = 1/10^{11} Pa; 1 Pa = 1 N/m^2
 Voigt approximation:
 Bulk modulus  B =    224.11157 kbar
 Young modulus E =    329.14136 kbar
 Shear modulus G =    131.10850 kbar
 Poisson Ratio n =      0.25523
 Reuss approximation:
 Bulk modulus  B =    224.11157 kbar
 Young modulus E =    302.94704 kbar
 Shear modulus G =    118.83024 kbar
 Poisson Ratio n =      0.27471
 Voigt-Reuss-Hill average of the two approximations:
 Bulk modulus  B =    224.11157 kbar
```

```
     Young modulus E =    316.04420 kbar
     Shear modulus G =    124.96937 kbar
     Poisson Ratio n =      0.26449
     Voigt-Reuss-Hill average; sound velocities:
     Compressional V_P =     3051.797 m/s
     Bulk          V_B =     2311.241 m/s
     Shear         V_G =     1725.897 m/s
     The approximate Debye temperature is      174.272 K
    This run was terminated on:  21: 4:36  24Jan2023
  =   JOB DONE.
MPI processes are distributed on     2 nodes
     R & G space division:  proc/nbgrp/npool/nimage =48
     Reading input from _temporary_1
   Info: using nr1, nr2, nr3 values from input
   Computing the elastic constants at the minimum volume
   FFT mesh: (   72,   72,   72 )
     Bravais lattice:
     ibrav=  1: simple cubic
     Cell parameters:
     alat=  10.597100 a.u.
   Starting primitive lattice vectors:
     crystal axes: (cart. coord. in units of alat)
          a(1) = (   1.000000   0.000000   0.000000 )
           a(2) = (   0.000000   1.000000   0.000000 )
           a(3) = (   0.000000   0.000000   1.000000 )
    Starting reciprocal lattice vectors:
     reciprocal axes: (cart. coord. in units 2 pi/alat)
          b(1) = (  1.000000  0.000000  0.000000 )
           b(2) = (  0.000000  1.000000  0.000000 )
           b(3) = (  0.000000  0.000000  1.000000 )
     Starting atomic positions in Cartesian axes:
     site n.     atom                  positions (alat units)
         1           Cs  tau(   1) = (   0.0000000   0.0000000   0.0000000  )
         2           Ge  tau(   2) = (   0.5000000   0.5000000   0.5000000  )
         3           Br  tau(   3) = (   0.5000000   0.5000000   0.0000000  )
```

```
              4          Br  tau(   4) = (   0.5000000   0.0000000   0.5000000  )
              5          Br  tau(   5) = (   0.0000000   0.5000000   0.5000000  )
           Starting atomic positions in crystallographic axes:
  Program PWSCF v.6.4.1 begins on 31Jan2023 at 20:42:52
          MPI processes distributed on     2 nodes
          R & G space division:  proc/nbgrp/npool/nimage =48
           Reading input from _temporary_1
         Info: using nr1, nr2, nr3 values from input
        Computing the elastic constants at the minimum volume
         FFT mesh: (   72,   72,   72 )
           Bravais lattice:
           ibrav=  1: simple cubic
           Cell parameters:
           alat=  10.597100 a.u.
         Starting primitive lattice vectors:
           crystal axes: (cart. coord. in units of alat)
                  a(1) = (   1.000000   0.000000   0.000000 )
                   a(2) = (   0.000000   1.000000   0.000000 )
                   a(3) = (   0.000000   0.000000   1.000000 )
          Starting reciprocal lattice vectors:
           reciprocal axes: (cart. coord. in units 2 pi/alat)
     Min 70 35 10 3122 1101 170
      Max 71 36 11 3131 1106 175
      Aggregate 3397 1701 489 150117 52923 8217
       bravais-cross section list = 1
      cross-section boundary (alat) = 10.3593 a.u.
      unit-cell volume = 1111.7093 (a.u.)^3
      number of iotas/cell = 5
      number of nuclear kinds = 3
      number of electrons = 34.00
      number of Kohn-Joke states= 200
      active energy cutoff = 50.0000 Ry
      charge thickness cutoff = 400.0000 Ry
```

Appendix VI: Output File for CsSiBr3 Elastic Constants

```
      Program PWSCF v.6.4.1 begins on 31Jan2023 at 20:42:52
       MPI processes distributed on     2 nodes
       R & G space division:  proc/nbgrp/npool/nimage =48
        Reading input from _temporary_1
     Info: using nr1, nr2, nr3 values from input
     Computing the elastic constants at the minimum volume
     FFT mesh: (   72,   72,   72 )
        Bravais lattice:
        ibrav=  1: simple cubic
        Cell parameters:
        alat=  10.597100 a.u.
     Starting primitive lattice vectors:
        crystal axes: (cart. coord. in units of alat)
              a(1) = (   1.000000   0.000000   0.000000 )
               a(2) = (   0.000000   1.000000   0.000000 )
               a(3) = (   0.000000   0.000000   1.000000 )
       Starting reciprocal lattice vectors:
        reciprocal axes: (cart. coord. in units 2 pi/alat)
 Min 70 35 10 3122 1101 170
  Max 71 36 11 3131 1106 175
  Aggregate 3397 1701 489 150117 52923 8217
   bravais-cross section list = 1
  cross-section boundary (alat) = 10.3593 a.u.
  unit-cell volume = 1111.7093 (a.u.)^3
  number of iotas/cell = 5
  number of nuclear kinds = 3
  number of electrons = 34.00
  number of Kohn-Joke states= 200
  active energy cutoff = 50.0000 Ry
  charge thickness cutoff = 400.0000 Ry
  Trade relationship = PBE ( 1 4 3 4 0 0)
  celldm(1)= 10.359300 celldm(2)= 0.000000 celldm(3)= 0.000000
```

```
celldm(4)= 0.000000 celldm(5)= 0.000000 celldm(6)= 0.000000
precious stone tomahawks: (truck. coord. in units of alat)
          a(1) = ( 1.000000 0.000000 0.000000 )
          a(2) = ( 0.000000 1.000000 0.000000 )
          a(3) = ( 0.000000 0.000000 1.000000 )
equal tomahawks: (truck. coord. in units 2 pi/alat)
          b(1) = ( 1.000000 0.000000 0.000000 )
          b(2) = ( 0.000000 1.000000 0.000000 )
       Called by h_psi:
       h_psi:pot    :     77.80s CPU     80.41s WALL (    3436 calls)
       h_psi:calbec :      2.33s CPU      2.38s WALL (    3436 calls)
       vloc_psi     :     74.15s CPU     76.71s WALL (    3436 calls)
       add_vuspsi   :      1.31s CPU      1.31s WALL (    3436 calls)
       General routines
       calbec       :      2.33s CPU      2.37s WALL (    3436 calls)
       fft          :      0.01s CPU      0.01s WALL (      13 calls)
       ffts         :      0.00s CPU      0.00s WALL (       1 calls)
       fftw         :     72.24s CPU     74.31s WALL (  916496 calls)
       interpolate  :      0.00s CPU      0.00s WALL (       1 calls)
       davcio       :      0.07s CPU      0.18s WALL (     324 calls)
        Parallel routines
       fft_scatt_xy :      1.89s CPU      2.63s WALL (  916510 calls)
       fft_scatt_yz :     61.70s CPU     60.33s WALL (  916510 calls)
        PWSCF        :  11m55.54s CPU  12m19.89s WALL
     This run was terminated on:  20:55:12  31Jan2023

  =------------------------------------------------------------------------------=
```

Appendix VII: Output File for Electronic Band Structure

```
Program PWSCF v.6.4.1 starts on 25Jan2023 at  5:20:44
        This program is part of the open-source Quantum ESPRESSO suite
        for quantum simulation of materials; please cite
           "P. Giannozzi et al., J. Phys.:Condens. Matter 21 395502 (2009);
           "P. Giannozzi et al., J. Phys.:Condens. Matter 29 465901 (2017);
            URL http://www.quantum-espresso.org",
        in publications or presentations arising from this work. More details at
        http://www.quantum-espresso.org/quote
        Parallel version (MPI), running on    48 processors
        MPI processes distributed on 2 nodes
        R & G space division:  proc/nbgrp/npool/nimage =      48
        Waiting for input...
        Reading input from standard input
        Current dimensions of program PWSCF are:
        Max number of different atomic species (ntypx) = 10
        Max number of k-points (npk) =  40000
        Max angular momentum in pseudopotentials (lmaxx) =  3
        Atomic positions and unit cell read from directory:
        ./out/aiida.save/
         Subspace diagonalization in iterative solution of the eigenvalue problem:
        one subgroup per band group will be used
        scalapack distributed-memory algorithm (size of sub-group:  4*  4 procs)

        Parallelization info
        --------------------
        sticks:   dense  smooth     PW     G-vecs:    dense   smooth      PW
        Min          74      37     10                3346     1177     180
        Max          75      38     11                3351     1183     185
        Sum        3569    1781    509              160707    56667    8733
         bravais-lattice index     =            1
        lattice parameter (alat)  =      10.5971  a.u.
        unit-cell volume          =    1190.0387 (a.u.)^3
```

```
number of atoms/cell      =            5
number of atomic types    =            3
number of electrons       =        44.00
number of Kohn-Sham states=          200
kinetic-energy cutoff     =      50.0000  Ry
charge density cutoff     =     400.0000  Ry
Exchange-correlation      =  SLA  PW   PBX  PBC ( 1  4  3  4 0 0)
celldm(1)=  10.597100  celldm(2)=   0.000000  celldm(3)=   0.000000
celldm(4)=   0.000000  celldm(5)=   0.000000  celldm(6)=   0.000000
crystal axes: (cart. coord. in units of alat)
          a(1) = (   1.000000   0.000000   0.000000 )
          a(2) = (   0.000000   1.000000   0.000000 )
          a(3) = (   0.000000   0.000000   1.000000 )
reciprocal axes: (cart. coord. in units 2 pi/alat)
          b(1) = (  1.000000  0.000000  0.000000 )
          b(2) = (  0.000000  1.000000  0.000000 )
          b(3) = (  0.000000  0.000000  1.000000 )
PseudoPot # 1 for Br read from file:
/mnt/lustre/users/mnamisi/ken/pseudos/br_pbe_v1.4.uspp.F.UPF
MD5 checksum: d3ffb7b29f6225aa16fe06858fb2a80b
Pseudo is Ultrasoft + core correction, Zval =  7.0
Generated by new atomic code, or converted to UPF format
Using a radial grid of  879 points,  6 beta functions with:
        http://www.quantum-espresso.org/quote
Parallel version (MPI), running on    48 processors
MPI processes are distributed on 2 nodes
R & G space division:  proc/nbgrp/npool/nimage =      48
Waiting for input...
Reading input from standard input
Current dimensions of the program PWSCF are:
Max number of different atomic species (ntypx) = 10
Max number of k-points (npk) =  40000
Max angular momentum in pseudopotentials (lmaxx) =  3
Atomic positions and unit cell read from directory:
```

```
./out/aiida.save/
 Subspace diagonalization in iterative solution of the eigenvalue problem:
one subgroup per band group will be used
scalapack distributed-memory algorithm (size of sub-group:  4*  4 procs)
PseudoPot # 2 for Cs read from file:
/mnt/lustre/users/mnamisi/ken/pseudos/Cs_pbe_v1.uspp.F.UPF
MD5 checksum: 3476d69cb178dfad3ffaa59df4e07ca4
Pseudo is Ultrasoft + core correction, Zval =  9.0
Generated by new atomic code, or converted to UPF format
Using a radial grid of  905 points,  6 beta functions with:
          l(1) =   0
          l(2) =   0
          l(3) =   1
          l(4) =   1
          l(5) =   2
          l(6) =   2
Q(r) pseudized with  6 coefficients,  rinner =    1.500   1.500   1.500
                                                  1.500   1.500
PseudoPot # 3 for Ge read from file:
/mnt/luster/users/mnamisi/ken/pseudos/ge_pbe_v1.4.uspp.F.UPF
MD5 checksum: 9c9eaa91e581c3f09632fb3098b2c6b2
Pseudo is Ultrasoft + core correction, Zval = 14.0
Generated by new atomic code, or converted to UPF format
Using a radial grid of  873 points,  6 beta functions with:
          l(1) =   0
          l(2) =   0
          l(3) =   1
          l(4) =   1
          l(5) =   2
          l(6) =   2
Q(r) pseudized with  8 coefficients,  rinner =    1.400   1.400   1.400
                                                  1.400   1.400
atomic species   valence    mass     pseudopotential
   Br             7.00    79.90400     Br( 1.00)
```

```
     Cs            9.00    132.90545     Cs( 1.00)
     Ge           14.00     72.64000     Ge( 1.00)
       Called by sum_band:
    Called by *egterg:
    h_psi        :     72.35s CPU     74.88s WALL (    3460 calls)
    s_psi        :      1.60s CPU      1.60s WALL (    3460 calls)
    g_psi        :      0.44s CPU      0.44s WALL (    3106 calls)
    cdiaghg      :    500.78s CPU    511.14s WALL (    3268 calls)
    cegterg:over :     30.81s CPU     31.75s WALL (    3106 calls)
    cegterg:upda :     18.68s CPU     18.76s WALL (    3106 calls)
    cegterg:last :     13.25s CPU     13.29s WALL (     678 calls)
    cdiaghg:chol :     25.00s CPU     25.64s WALL (    3268 calls)
    cdiaghg:inve :     28.78s CPU     29.02s WALL (    3268 calls)
    cdiaghg:para :     56.89s CPU     61.18s WALL (    6536 calls)
    Called by h_psi:
    h_psi:pot    :     72.08s CPU     74.60s WALL (    3460 calls)
    h_psi:calbec :      2.36s CPU      2.41s WALL (    3460 calls)
    vloc_psi     :     68.16s CPU     70.62s WALL (    3460 calls)
    add_vuspsi   :      1.55s CPU      1.56s WALL (    3460 calls)
    General routines
    calbec       :      2.36s CPU      2.41s WALL (    3460 calls)
    fft          :      0.01s CPU      0.01s WALL (      13 calls)
    ffts         :      0.00s CPU      0.00s WALL (       1 calls)
    fftw         :     66.33s CPU     68.22s WALL (  908854 calls)
    interpolate  :      0.00s CPU      0.00s WALL (       1 calls)
    davcio       :      0.07s CPU      0.18s WALL (     324 calls)
     Parallel routines
    fft_scatt_xy :      1.75s CPU      2.61s WALL (  908868 calls)
    fft_scatt_yz :     55.78s CPU     53.98s WALL (  908868 calls)
     PWSCF        :  11m 0.76s CPU  11m24.44s WALL
   This run was terminated on:   5:32: 8  25Jan2023
=------------------------------------------------------------------------------=
```

Appendix VIII: Output File for Optical Properties

This software is an integral component of the open-source Quantum ESPRESSO suite, which facilitates quantum simulations of materials. For any publications or presentations that result from the use of this program, please reference the following works: "P. Giannozzi et al., J. Phys.: Condens. Matter 21 395502 (2009);" and "P. Giannozzi et al., J. Phys.: Condens. Matter 29 465901 (2017);" along with the URL http://www.quantum-espresso.org. Additional information can be found at http://www.quantum-espresso.org/quote. The parallel version of this program, utilizing MPI, is currently operating on 48 processors, with the MPI processes distributed across 2 nodes. The division of R & G space is configured as proc/nbgrp/npool/nimage = 48. The program is now awaiting input and is reading from the standard input. The current specifications for the PWSCF program are as follows: the maximum number of distinct atomic species (ntypx) is 10, the maximum number of k-points (npk) is 40,000, and the maximum angular momentum in pseudopotentials (lmaxx) is 3. Atomic positions and the unit cell have been retrieved from the directory: ./out/aiida.save/. In the iterative solution of the eigenvalue problem, subspace diagonalization will employ one subgroup per band group, utilizing a ScaLAPACK distributed-memory algorithm with a subgroup size of 4 * 4 processors.

> The information regarding parallelization has been generated using the Vanderbilt code, version 7.3.6, authored by kfg, with the generation date recorded as May 13, 2013. The original format has been automatically converted, and the Pseudo was produced through a Scalar-Relativistic Calculation. The local potential cutoff radius is specified as 2.30000000000E+00, with various parameters such as nl, pn, l, occupancy, Rcut, Gcut, and pseudopotential values detailed for different orbital types, including 5S, 5P, 5D, 6S, and 6P.

The header section provides essential details, including the version number, the element being analyzed (Cs), and the type of pseudopotential employed (Ultrasoft). It also indicates the presence of a Nonlinear Core Correction and specifies the exchange-correlation functional used, which is the PBE. The valence Z is noted as 9.00000000000, with the total energy calculated at -63.00384417630. Suggested cutoffs for wavefunctions and charge density are both indicated as 0.00000, while the maximum angular momentum component is set at 2, and the mesh comprises 905 points. The number of wavefunctions and projectors is recorded as 5 and 6, respectively, with detailed occupancy values for the various wavefunctions.

The mesh section outlines the radial coordinates, beginning from 0.00000000000E+00 and extending to 5.67720230969E-06, providing a comprehensive range of values. Additionally, the PP_DIJ subsection lists the number of nonzero Dij values, which totals nine. Each entry specifies the indices and corresponding Dij values, illustrating the interactions between different components, with notable values such as 1.29207215929E+00, -1.76637262031E+00, and 1.39232024315E+00, among others, reflecting the complexity of the system being analyzed.

Appendix IX: KUREC Clearance Letter

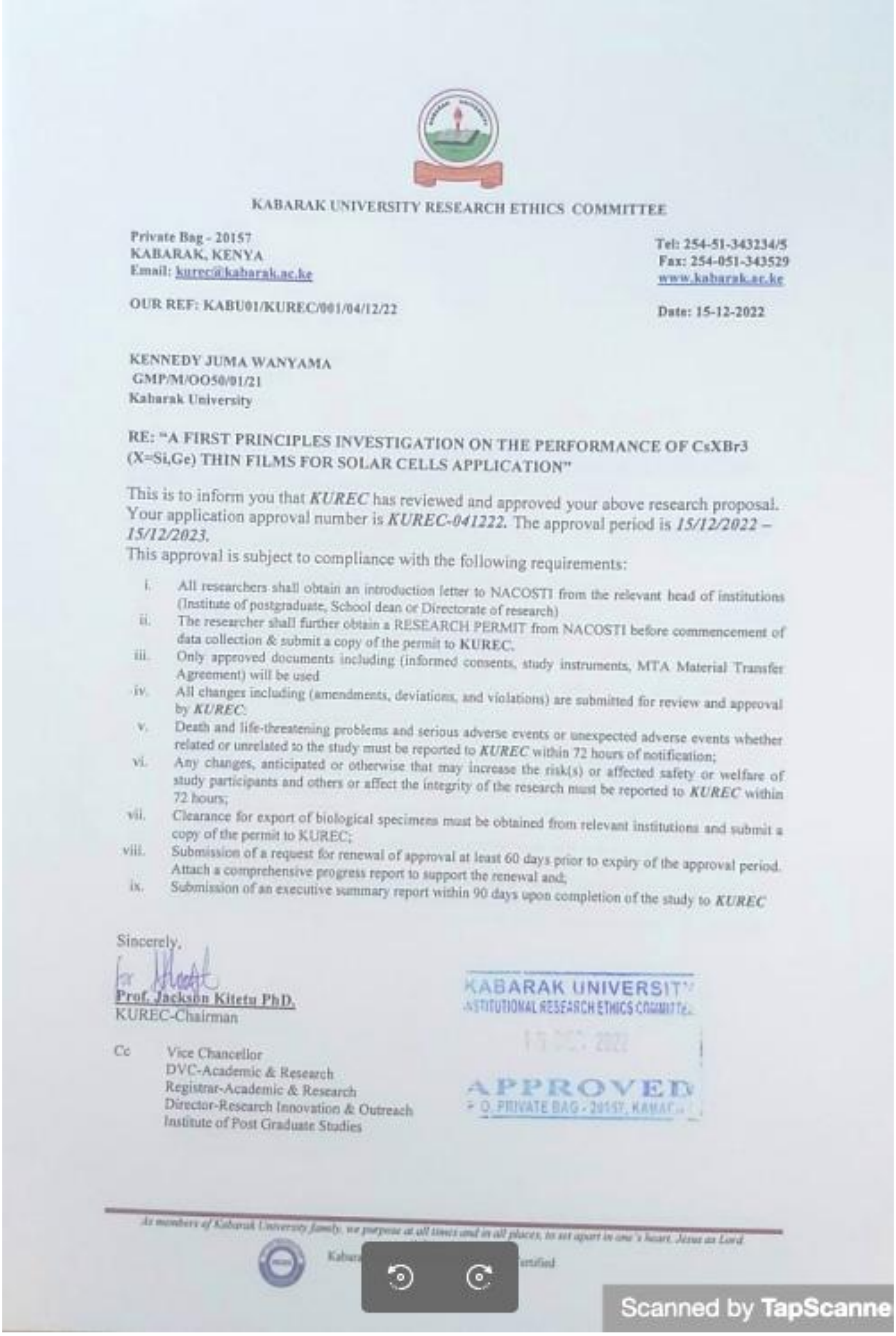

KABARAK UNIVERSITY RESEARCH ETHICS COMMITTEE

Private Bag - 20157
KABARAK, KENYA
Email: kurec@kabarak.ac.ke

Tel: 254-51-343234/5
Fax: 254-051-343529
www.kabarak.ac.ke

OUR REF: KABU01/KUREC/001/04/12/22

Date: 15-12-2022

KENNEDY JUMA WANYAMA
GMP/M/OO50/01/21
Kabarak University

RE: "A FIRST PRINCIPLES INVESTIGATION ON THE PERFORMANCE OF CsXBr3 (X=Si,Ge) THIN FILMS FOR SOLAR CELLS APPLICATION"

This is to inform you that ***KUREC*** has reviewed and approved your above research proposal. Your application approval number is ***KUREC-041222.*** The approval period is ***15/12/2022 – 15/12/2023.***

This approval is subject to compliance with the following requirements:

i. All researchers shall obtain an introduction letter to NACOSTI from the relevant head of institutions (Institute of postgraduate, School dean or Directorate of research)
ii. The researcher shall further obtain a RESEARCH PERMIT from NACOSTI before commencement of data collection & submit a copy of the permit to KUREC.
iii. Only approved documents including (informed consents, study instruments, MTA Material Transfer Agreement) will be used
iv. All changes including (amendments, deviations, and violations) are submitted for review and approval by ***KUREC***;
v. Death and life-threatening problems and serious adverse events or unexpected adverse events whether related or unrelated to the study must be reported to ***KUREC*** within 72 hours of notification;
vi. Any changes, anticipated or otherwise that may increase the risk(s) or affected safety or welfare of study participants and others or affect the integrity of the research must be reported to ***KUREC*** within 72 hours;
vii. Clearance for export of biological specimens must be obtained from relevant institutions and submit a copy of the permit to KUREC;
viii. Submission of a request for renewal of approval at least 60 days prior to expiry of the approval period. Attach a comprehensive progress report to support the renewal and;
ix. Submission of an executive summary report within 90 days upon completion of the study to ***KUREC***

Sincerely,

for

Prof. Jackson Kitetu PhD.
KUREC-Chairman

KABARAK UNIVERSIT
STITUTIONAL RESEARCH ETHICS COMMITTE
15 DEC 2022
APPROVED
O. PRIVATE BAG - 20157, KABAR

Cc
Vice Chancellor
DVC-Academic & Research
Registrar-Academic & Research
Director-Research Innovation & Outreach
Institute of Post Graduate Studies

As members of Kabarak University family, we purpose at all times and in all places, to set apart in one's heart, Jesus as Lord

Appendix X:NACOSTI Research Permit

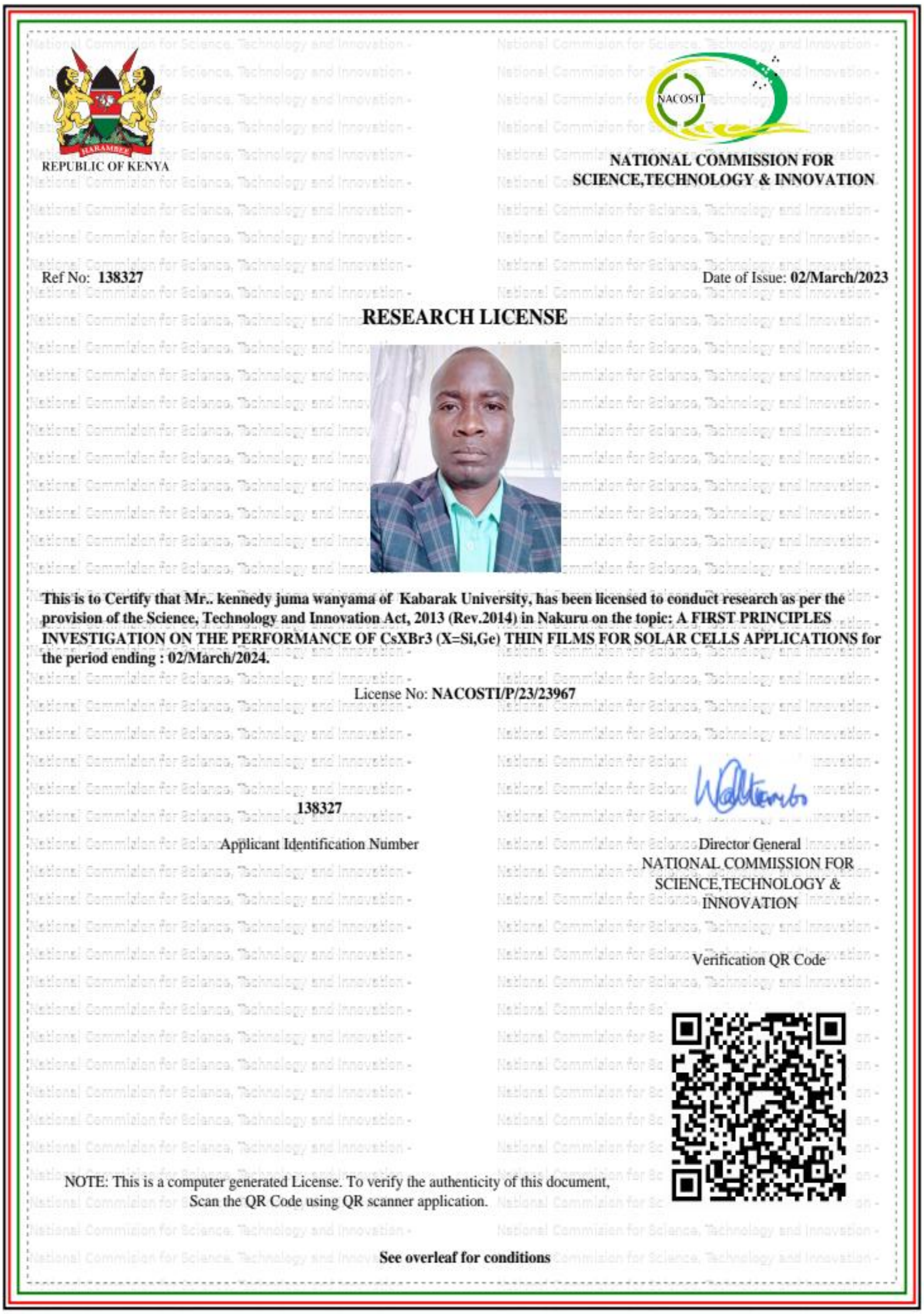

REPUBLIC OF KENYA

NATIONAL COMMISSION FOR
SCIENCE,TECHNOLOGY & INNOVATION

Ref No: **138327**

Date of Issue: **02/March/2023**

RESEARCH LICENSE

This is to Certify that Mr.. kennedy juma wanyama of Kabarak University, has been licensed to conduct research as per the provision of the Science, Technology and Innovation Act, 2013 (Rev.2014) in Nakuru on the topic: A FIRST PRINCIPLES INVESTIGATION ON THE PERFORMANCE OF CsXBr3 (X=Si,Ge) THIN FILMS FOR SOLAR CELLS APPLICATIONS for the period ending : 02/March/2024.

License No: **NACOSTI/P/23/23967**

138327

Applicant Identification Number

Director General
NATIONAL COMMISSION FOR
SCIENCE,TECHNOLOGY &
INNOVATION

Verification QR Code

NOTE: This is a computer generated License. To verify the authenticity of this document,
Scan the QR Code using QR scanner application.

See overleaf for conditions

Appendix XI: Evidence of Conference Participation

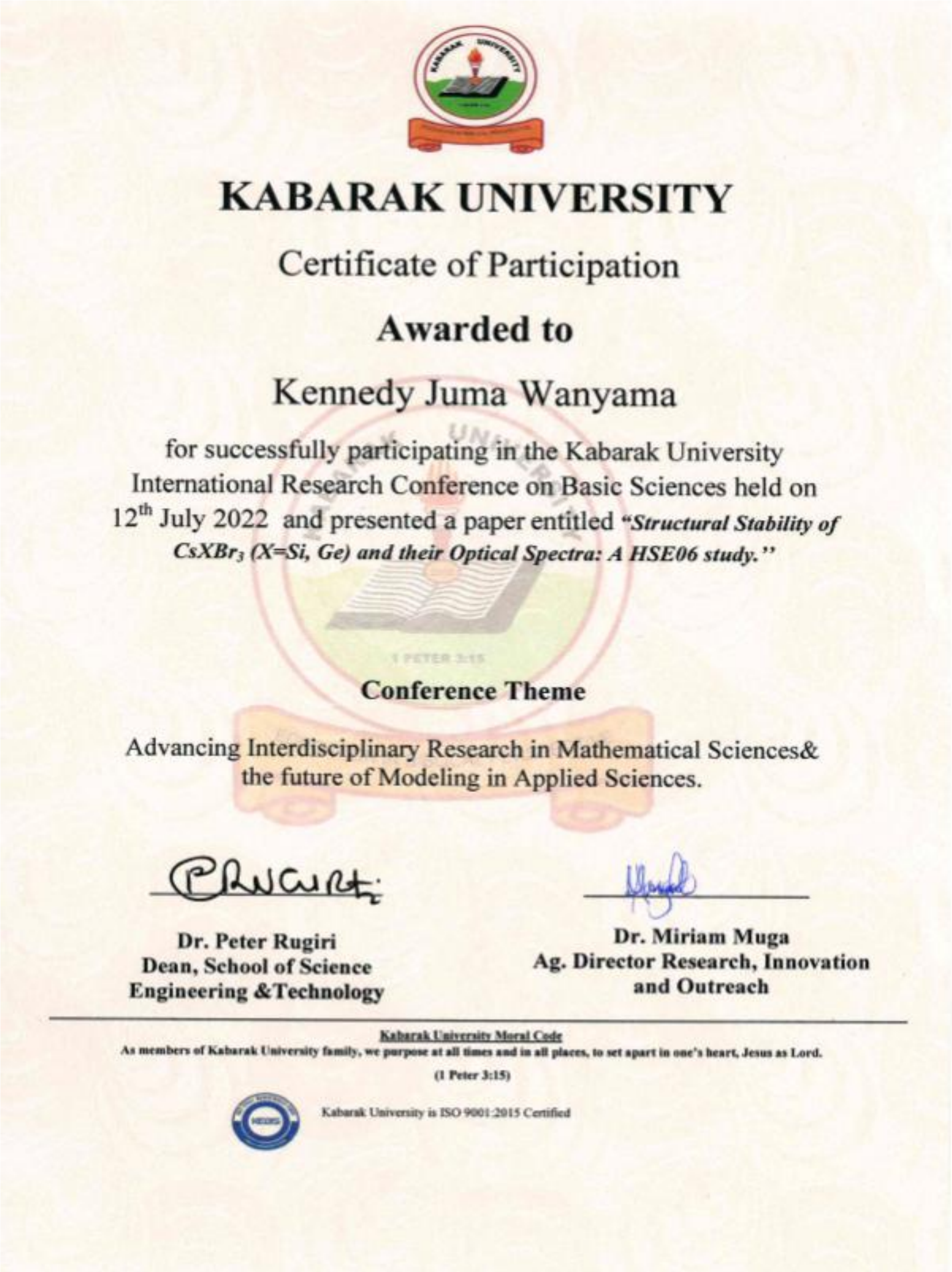

KABARAK UNIVERSITY

Certificate of Participation

Awarded to

Kennedy Juma Wanyama

for successfully participating in the Kabarak University International Research Conference on Basic Sciences held on 12th July 2022 and presented a paper entitled ***"Structural Stability of $CsXBr_3$ (X=Si, Ge) and their Optical Spectra: A HSE06 study."***

Conference Theme

Advancing Interdisciplinary Research in Mathematical Sciences& the future of Modeling in Applied Sciences.

Dr. Peter Rugiri
Dean, School of Science
Engineering &Technology

Dr. Miriam Muga
Ag. Director Research, Innovation
and Outreach

Kabarak University Moral Code

As members of Kabarak University family, we purpose at all times and in all places, to set apart in one's heart, Jesus as Lord.

(1 Peter 3:15)

Kabarak University is ISO 9001:2015 Certified

Appendix XII: List of Publication

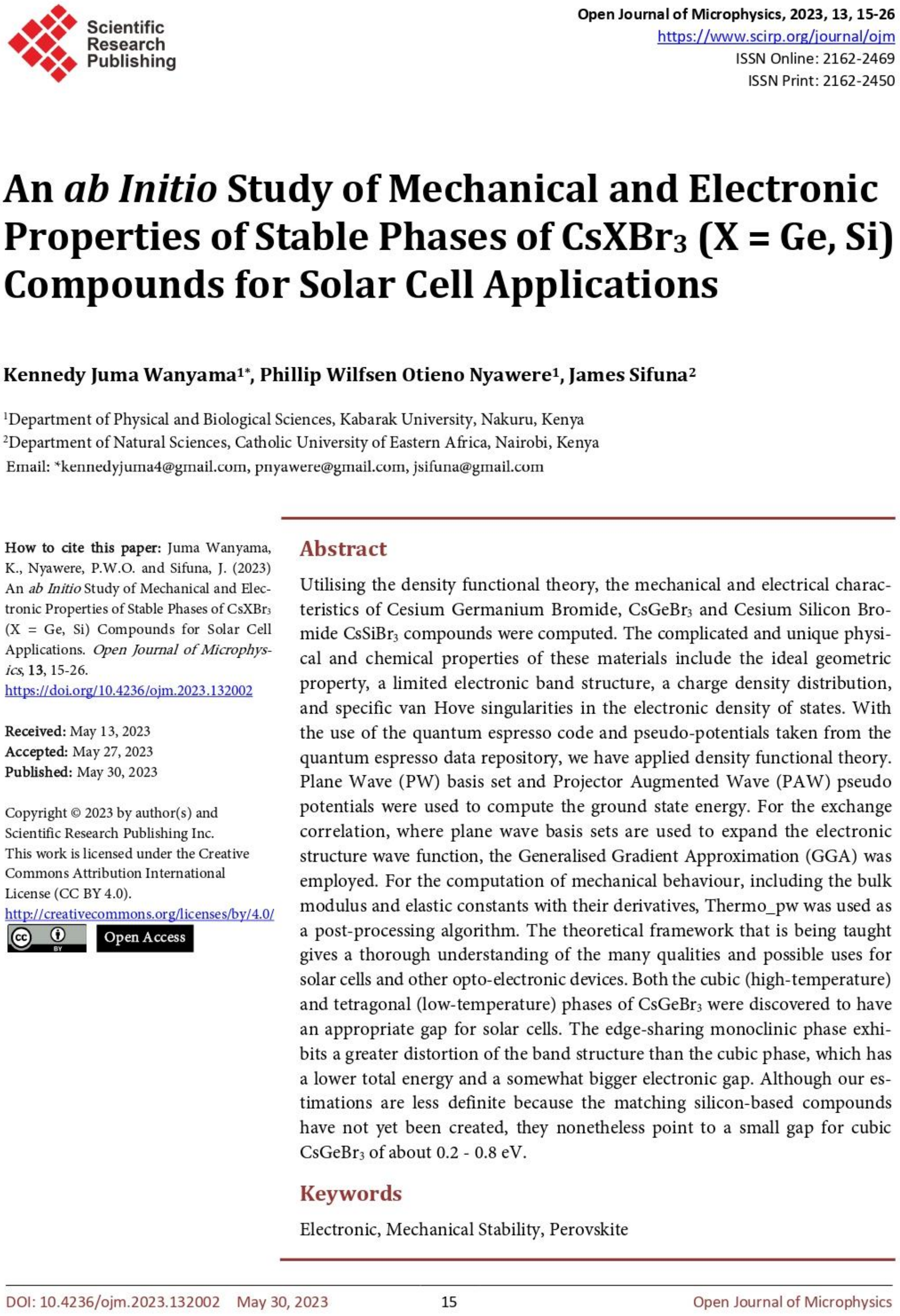

Scientific Research Publishing

Open Journal of Microphysics, 2023, 13, 15-26
https://www.scirp.org/journal/ojm
ISSN Online: 2162-2469
ISSN Print: 2162-2450

An *ab Initio* Study of Mechanical and Electronic Properties of Stable Phases of $CsXBr_3$ (X = Ge, Si) Compounds for Solar Cell Applications

Kennedy Juma Wanyama[1]*, Phillip Wilfsen Otieno Nyawere[1], James Sifuna[2]

[1]Department of Physical and Biological Sciences, Kabarak University, Nakuru, Kenya
[2]Department of Natural Sciences, Catholic University of Eastern Africa, Nairobi, Kenya
Email: *kennedyjuma4@gmail.com, pnyawere@gmail.com, jsifuna@gmail.com

How to cite this paper: Juma Wanyama, K., Nyawere, P.W.O. and Sifuna, J. (2023) An *ab Initio* Study of Mechanical and Electronic Properties of Stable Phases of $CsXBr_3$ (X = Ge, Si) Compounds for Solar Cell Applications. *Open Journal of Microphysics*, **13**, 15-26.
https://doi.org/10.4236/ojm.2023.132002

Received: May 13, 2023
Accepted: May 27, 2023
Published: May 30, 2023

Abstract

Utilising the density functional theory, the mechanical and electrical characteristics of Cesium Germanium Bromide, $CsGeBr_3$ and Cesium Silicon Bromide $CsSiBr_3$ compounds were computed. The complicated and unique physical and chemical properties of these materials include the ideal geometric property, a limited electronic band structure, a charge density distribution, and specific van Hove singularities in the electronic density of states. With the use of the quantum espresso code and pseudo-potentials taken from the quantum espresso data repository, we have applied density functional theory. Plane Wave (PW) basis set and Projector Augmented Wave (PAW) pseudo potentials were used to compute the ground state energy. For the exchange correlation, where plane wave basis sets are used to expand the electronic structure wave function, the Generalised Gradient Approximation (GGA) was employed. For the computation of mechanical behaviour, including the bulk modulus and elastic constants with their derivatives, Thermo_pw was used as a post-processing algorithm. The theoretical framework that is being taught gives a thorough understanding of the many qualities and possible uses for solar cells and other opto-electronic devices. Both the cubic (high-temperature) and tetragonal (low-temperature) phases of $CsGeBr_3$ were discovered to have an appropriate gap for solar cells. The edge-sharing monoclinic phase exhibits a greater distortion of the band structure than the cubic phase, which has a lower total energy and a somewhat bigger electronic gap. Although our estimations are less definite because the matching silicon-based compounds have not yet been created, they nonetheless point to a small gap for cubic $CsGeBr_3$ of about 0.2 - 0.8 eV.

Keywords

Electronic, Mechanical Stability, Perovskite